Modeling of grain size effects on deformation behavior and product quality in progressive microforming by using CPFEM

Xu Tong[a], Y. Li[b]*, M.W. Fu[a]*

a Department of Mechanical Engineering, Research Institute for Advanced Manufacturing, The Hong Kong Polytechnic University, Hong Kong, China

b Thayer School of Engineering, Dartmouth College, Hanover, NH 03755, U.S.A

** Email: yan.li@dartmouth.edu; mmmwfu@polyu.edu.hk*

Abstract

Progressive microforming is widely recognized as one of the most efficient and desirable methods of mass production in micromanufacturing arena. By using finite element method (FEM) to predict mechanical response of materials that are fabricated using progressive microforming, it needs to account for the microstructure details and deformation/failure mechanisms of the materials. To address this issue, a crystal plasticity finite element method-cohesive zone model (CPFEM-CZM) was developed to resolve complex deformation and failure mechanisms during the progressive microforming process. This model offers novel physical insights into how the grain size affects the interplay between crystallographic slip and mechanical twinning, and further material deformation during sheet blanking. In this work, a hexagon socket part was manufactured from a brass CuZn32 sheet using a three-step progressive microforming system. Experiments were conducted and compared with both CPFEM-CZM and conventional FEM simulations with the aim of analyzing the size effects in uniaxial tensile tests and the progressive microforming process. This comparison was focused on stress and strain distribution, microstructure evolution, deformation load, product dimensions, undesirable geometries, and surface quality of the made parts. The findings of this investigation demonstrate that the CPFEM-CZM approach is more reliable than conventional FEM in resolving the deformation process, with a particular strength in predicting multiple shear bands and dead metal zones. Additionally, the CPFEM-CZM method demonstrates superior accuracy in predicting undesirable geometries such as hole and rollover defects in the microformed parts. In conclusion, this research facilitates the understanding of grain size effects on the deformation behavior in progressive microforming and presents a novel approach and strategy for modeling, prediction, and product quality assurance in complex micro deformation and forming processes.

Keywords: Grain size effect; Progressive microforming; Deformation behavior; Crystal plasticity; Cohesive zone model; Complex deformations.

1. Introduction

Microforming, a deformation-based micro-scaled manufacturing technique, has emerged as a highly

sophisticated and indispensable technology for making different micro parts and structures, such as microelectronics, aerospace components, and biomedicine [1-3]. Progressive microforming, as the term suggests, involves a series of sequential forming steps to produce micro-scaled components with intricate shapes directly from metal sheets. This method offers several notable advantages. Firestly, it overcomes challenges related to the positioning, transportation, and ejection of both the sheet metal and the preform. Additionally, it streamlines tooling design by enabling simultaneous execution of multiple operations, resulting in enhanced efficiency and significant time savings. [4, 5]. Despite the above advantages of progressive microforming, scattering in property and dimention was observed in fabricated components whenthe ratio of grain size (d) to sheet thickness (t) approaches or exceeds 1 [xxx]. This size effects (SEs) [6] significantly affect the manufacturing reliability and quality control. It has been reported that SEs can be induced by a few parameters, such as loading conditions, dimensional accuracy, geometry irregularity, and surface quality, etc. Hirota [9], who first proposed the concept of sheet extrusion for the fabrication of parts. He found that SEs exist when xxxx. Ghassemali et al. [12], who explored the two-step progressive microforming technology using copper sheets for the production of micro-pins, XXX. Fu and Chan [10, 11] developed a three-step progressive forming process to directly fabricate hollow flanged micro- and meso-scaled parts and explored the grain SEs in relation to load and fracture surface morphology. Furthermore, Meng et al. [13] and Zheng et al. [14] used similar four-step progressive microforming systems to make more complex parts, such as double-flanged and conical-flanged components. Specifically, they studied the grain SEs and sheet thickness SEs on the dimensional accuracy, geometry irregularity, and microstructure evolution. The aforementioned research has yielded several widely accepted findings. Firstly, for a given sheet thickness, larger grain size results in a lower load. Secondly, the scatter of final part dimensions is generally more pronounced for coarse-grained material. However, the effect of grain size on dimensional accuracy and geometry irregularity can vary greatly depending on the specific component and forming design. For example, the extrusion length in a flat plunger part increases with grain size [15], while the opposite trend has been observed in another micropart [7].

In order to accurately predict and mitigate the effects of SEs, it is crucial to establish an efficient simulation framework specifically tailored for progressive microforming. This framework is indispensable for enhancing the precision of the microforming process and ensuring the high quality

of manufactured parts. By enabling accurate and stable prediction and simulation during the initial design phase, the framework supports informed decision-making regarding micro-part and tooling design, process optimization, and quality control.

In recent years, the rapid development of the crystal plasticity finite element method (CPFEM) has provided researchers with a promising new tool to address the challenging issues of material deformation and processing [16-18]. Compared with conventional finite element method that assumes isotropy at the macroscale level, CPFEM can capture important microscale phenomenon, such as crystallographic grain orientations, dislocation interactions, and strain localization, which are important in understanding the root cause of property scattering and uncertainties in manufacturing.

Due to the relatively high computational cost associated with CPFEM simulation, representative volume elements (RVEs) are employed. Despite its economical nature and ability to be studied at the level of deformation mechanisms, this simplified method is not deemed suitable for the simulation of progressive microforming. In the field of progressive microforming, researchers often adopt a scaled simplified modeling approach to study key issues such as material flow and microstructure evolution. The wide applications of the CPFEM in the research on the deformations such as tension, compression, torsion, and bending are evident, while it was rarely utilized in the simulation of complex deformation processes. Cao et al. [21] attempted a forward extrusion simulation via the CPFEM, while Guo et al. [22] studied the SEs in micro deep drawing via a holistic model of a TWIP sheet and found consistent results with experiments and CPFEM simulations. Tong et al. [23] also validated the results of the CPFEM in a microembossing process of a multi-channel structure and found it to be a superior alternative to the conventional FEM. Therefore, the potential of the CPFEM to be applied to complex deformations can be seen. However, in progressive microforming, it is not just a matter of elastic and plastic deformation but often involves the material fracture behavior as well.

The examination of damage behavior within the domain of metallic materials has always been a topic with paramount significance, particularly in the arena of deformation-based manufacturing and materials processing. In recent years, the utilization of CPFEM-based methods to analyze the fracture

of materials has become a prevalent practice [24, 25]. The most common and effective approach for modeling the fracture of metallic materials is element elimination, which is predicated under the framework of continuum mechanics damage. In tandem with this, Liu et al. [26] integrated the CPFEM with three ductile fracture criteria (DFCs) based on the principal strain, the equivalent plastic strain, and the maximum shear strain, respectively, to simulate the micro-cutting process. Similarly, Wang et al. [27] used the Johnson-Cook damage model in conjunction with the CPFEM for the simulation of pure copper cutting. In a cross-scaled study, Zhang et al. [28] compared 10 uncoupled DFCs to examine the SEs of Inconel 718 superalloy. However, the strain experienced during progressive microforming can be substantial, as extrusion and fracture coexist in multiple processing steps, leading to excessive material loss and inaccurate simulation results if too many elements are deleted. In such a way, another model that does not rely on the element deletion method enters the view of researchers, namely, the cohesive zone model (CZM). In finite element analysis, CZM refers to the insertion of cohesive elements with or without thickness between the desired material elements, allowing for the separation of elements to occur without affecting the overall material volume when the cohesive elements are deleted [29]. The combination of CPFEM and CZM methods was first proposed by Xu and Needleman [30] and has gained popularity in recent years. Phan et al. [31] applied the CPFEM-CZM method to study the creep and rupture deformation, and only embedded cohesive elements between grains to simulate intergranular failure. Zhao et al. [32] and Yalçinkaya et al. [33] also used this combining method to analyze intergranular fracture in creep-fatigue and tension deformation, respectively. However, for common metals such as copper and brass, merely intergranular cracking is inadequate and imprecise in characterizing the material fracture behavior in progressive microforming., as intragranular cracking must also be considered. Liu et al. [34] investigated the crystal cracking of aluminum sheets through a simulation based on the CPFEM-CZM method that utilized full-field cohesive elements. The simulation creatively modeled the fracture of single-crystal and bi-crystal Al through molecular dynamic methods to determine intracrystalline and grain boundary damage laws, providing the cohesion parameters for the CPFEM-CZM simulation. Therefore, the COFEM-CZM can be utilized to complex deformations represented by progressive microforming, however, one of the key issues is how to apply it.

In this work, a novel CPFEM-CZM method is developed to simulate the complex deformation behaviors induced by SEs in progressive microforming. In this method, CPFEM is employed to elucidate how grain size affects the interplay between crystallographic slip and mechanical twinning, as well as additional material deformation during sheet blanking. CZM explicitly resolves the fracture initiation and propogation based on the grain-level deformation. As a case study, a hexagonal socket component frequently utilized in electronic devices was selected, and a progressive microforming system comprising three operations of two-step extrusion and one-step blanking using CuZn32 sheets was developed. Sheets with t = 1 mm and d = 17.5-157.7 μm were subjected to uniaxial tensile tests and hexagonal socket product processing. The CPFEM was established with a polycrystalline geometric model of sheets with actual texture. The deviations in product quality and mechanical responses induced by grain SEs were then analyzed by comparing the results obtained from FEM simulation, CPFEM-CZM simulation, and experiments, encompassing strain patterns, load-stroke curves, dimensional accuracy, undesirable geometry, surface defects, and surface roughness.

2. Experimental methodology

2.1. Testing materials

To thoroughly investigate the grain SEs, the material was subjected to a range of heat treatments with varying conditions, including 450℃-1h, 600℃-1h, and 700℃-2h. Microstructural observations were made through both optical microscopy and electron backscatter diffraction (EBSD), as depicted in **Fig. 1**. The composition of the brass CuZn32 sheet is shown in **Table 1**. The samples were cut, polished, and then etched for 8-10s, while those intended for EBSD examination underwent electrolytic polishing. The acquisition and analysis of images were executed using the HKL 5-channel software package in conjunction with the EBSD system, with step size parameter of 1 μm and 2.5 μm, respectively. Data from the EBSD tests were utilized in the crystal plasticity model as described in Section 3.1. subsequent simulations involving crystal plasticity finite element (CPFE) methods, enabling more accurate determination of average grain sizes for modeling and constitutive model calibration purposes. In this study, CuZn32 sheets with varying average grain size of 17.5 μm, 62.1 μm, and 157.7 μm were utilized in both uniaxial tensile tests in Section 2.2 and progressive

microforming process in Section 2.3.

Table 1 Chemical composition of the as-received CuZn32 sample.

Content (mass fraction, %)						
Cu	Fe	Sb	Bi	P	Pb	Zn
67.50	0.1	0.005	0.002	0.01	0.03	Bal.

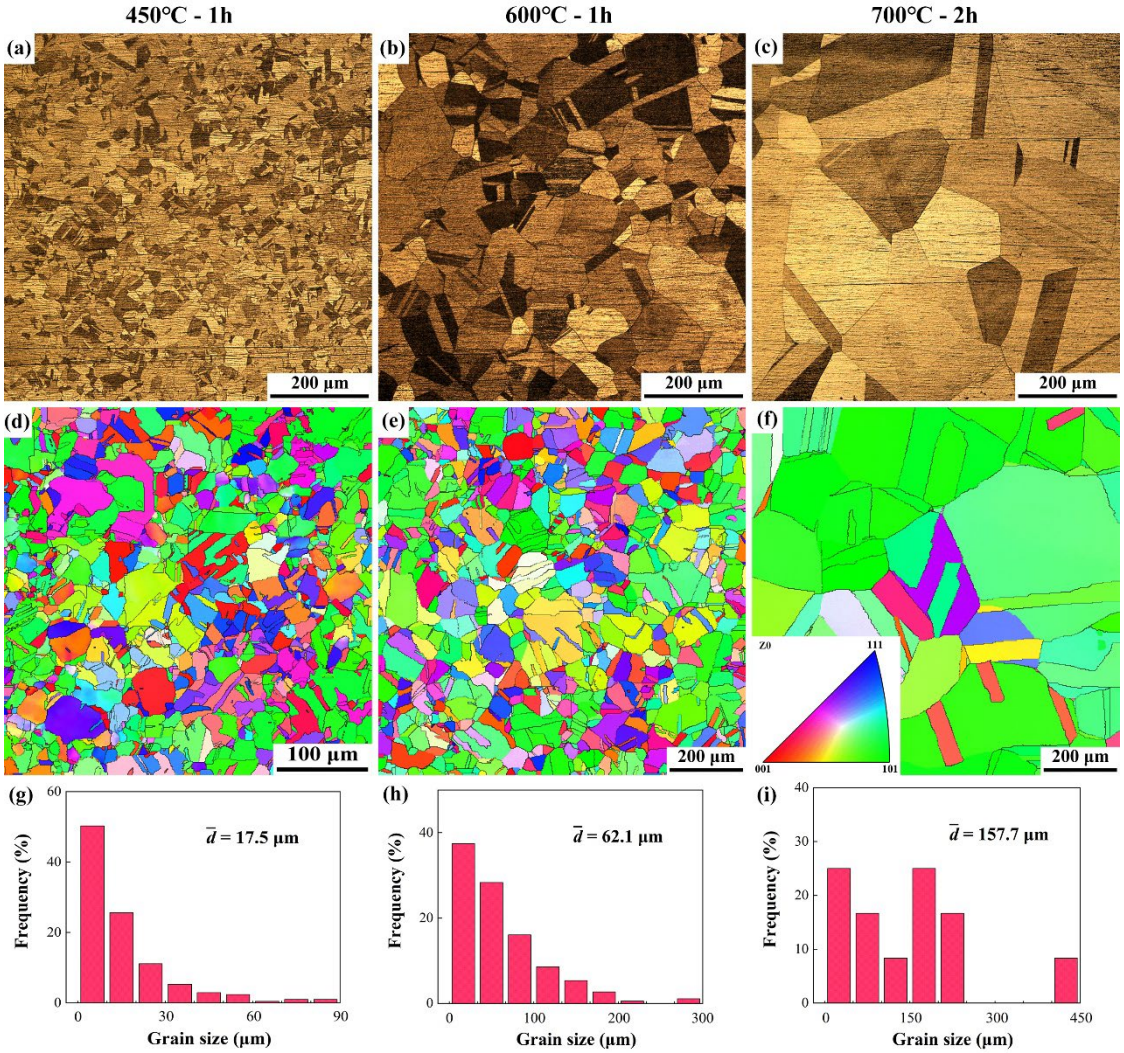

Fig. 1. (a-c) The initial microstructure and (d-f) EBSD grain orientation mappings of the CuZn32 sheets under heat treatment conditions of 450°C-1h, 600°C-1h, and 700°C-2h; (g-i) grain size distribution in three specimens with the average grain sizes of 17.5, 62.1, and 157.7 μm, respectively.

2.2. Uniaxial tensile test

The uniaxial tensile tests were conducted using a programmable MTS testing machine and an extensometer on CuZn32 sheets with a strain rate of 0.001 s^{-1} at room temperature. The objective of the experiments is to find the correlations between grain size and the true stress of the specimens. The correlation was integrated into both the conventional FEM framework and the CPFEM-CZM framework. Test setup and sample configurations follow the ASTM: E8/E8M standards. The stress-strain data from three groups of specimens were averaged for each grain size. As depicted in **Fig. 2(a)**, the specimen with coarser grain corresponds to a lower true stress response and therefore leads to lower initial yield stress due to the reduced grain boundary strengthening effect. Moreover, the coarser-grained specimen tends to be more brittle as the fracture strain decreases with increasing grain size. Since α-brass is one typical FCC metallic material with low stacking fault energy, deformation twinning plays a vital role in CuZn32 microstructure evolution. In the initial stage of deformation, specimens with fine grains exhibit a higher strain hardening rate due to the severe impediment of dislocation movement at the grain boundaries. This trend does not hold when the truss stress goes beyond a threshold. As indicated in **Fig. 2(b)**, the specimen with the largest grain size (157.7 μm) starts to exhibit a higher work hardening rate than its counterpart with 62.1 μm grain size when the true stress is beyond 300 MPa. Deformation twinning generates an additional hardening mechanism. The correlation between work hardening and twinning can be ascribed to three factors, as elucidated in **Fig. 1(d-f)**: (1) twinning activates the grain splitting, reduces the effective distance of dislocation slip, and facilities strain hardening by the Hall-Petch effect; (2) twinning changes the lattice orientation; and (3) twin region in a less strained matrix is harder than the adjacent non-twin region within a grain according to the Baczynski hardening mechanism [35].

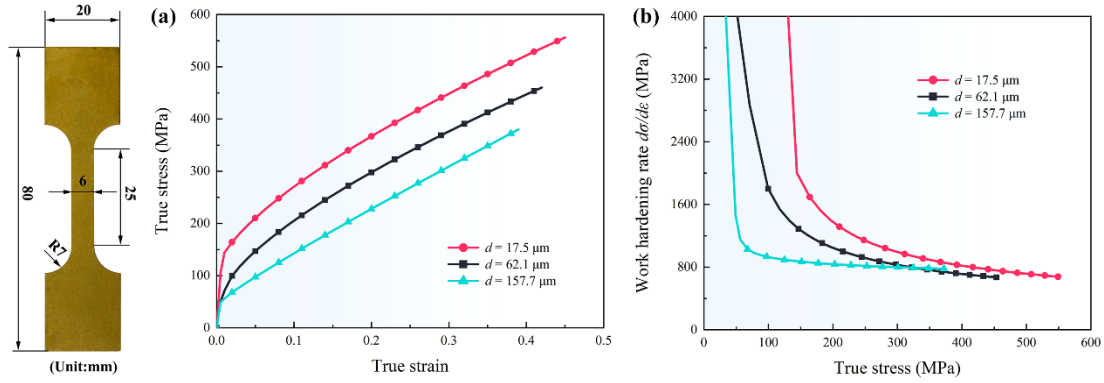

Fig. 2. (a) The true stress-strain relations and (b) work hardening curves obtained from the uniaxial tensile tests with various grain sizes of brass CuZn32.

2.3. Progressive microforming process

A hexagonal socket part as shown in **Fig. 3(c)** was fabricated using progressive microforming. A set of these socket parts, often of similar geometric configuration, are commonly produced via turning or extrusion processes. This approach can lead to high-quality products with high efficiency. The tooling system utilized in the study, as illustrated in **Fig. 3(a)**, consists of a platform, a blank holder, a die holder, a bottom plate, and three sets of punch and die. All the components were made of Cr12 cold-work die steel. During the microforming process, an 80 mm × 20 mm × 1 mm brass sheet was fed through the system from left to right by 20 mm per step. The final product was deposited on the bottom plate after two forward extrusion steps and a blanking step. In Step I, a punch with a 1 mm radius was employed to effect a 0.6 mm movement along the thickness direction. As a result, the material is extruded into a 0.5 mm radius tunnel with a 0.2 mm-45° chamfer. If a columnar material is employed, the extrusion ratio at this stage would reach 2. In Step II, a hexagon socket with 0.25 mm thickness and 0.8 mm diagonal distance was formed via forward extrusion at the top of the material. Step III involved a complete cutting of the part via a punch with a 0.8 mm radius. A uniform slow punch speed of 0.005 mm/s was employed to eliminate the impact of strain rate in all the three steps. The resulting microparts are shown in **Fig. 3(d)**.

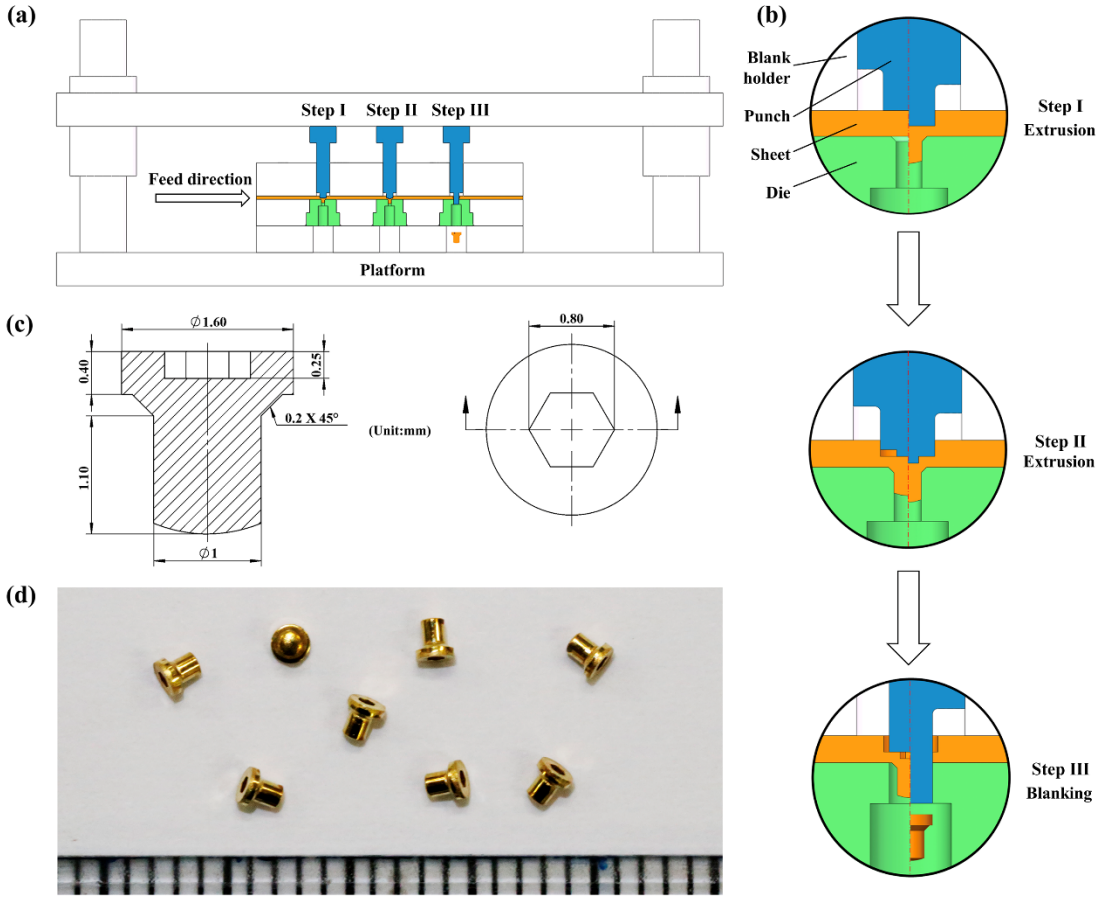

Fig. 3. (a) Progressive microforming system; (b) illustration of the forming steps; (c) design of the hexagon socket part; and (d) the fabricated part with various grain sizes.

3. CPFEM-CZM method and modeling details

3.1. Crystal plasticity constitutive model

The total deformation gradient $\boldsymbol{F}$, imparted upon a crystalline material by means of crystal slip and twinning, can be decomposed into two constituent parts: the plastic deformation gradient $\boldsymbol{F}^p$ (from slip and deformation twinning) and the elastic deformation gradient $\boldsymbol{F}^e$ (from the reversible stretching and rotation of the crystal lattice):

$$\boldsymbol{F} = \boldsymbol{F}^e \cdot \boldsymbol{F}^p = \boldsymbol{F}^e \cdot \boldsymbol{F}^{twin} \cdot \boldsymbol{F}^{slip}. \tag{1}$$

The velocity gradient tensor $\boldsymbol{L}$ can be composed of the elastic deformation velocity gradient tensor $\boldsymbol{L}^e$ and the plastic deformation velocity gradient tensor $\boldsymbol{L}^p$ as:

$$\boldsymbol{L} = \dot{\boldsymbol{F}} \cdot \boldsymbol{F}^{-1} = \dot{\boldsymbol{F}}^{e} \cdot \boldsymbol{F}^{e\,-1} + \boldsymbol{F}^{e} \cdot \dot{\boldsymbol{F}}^{p} \cdot \boldsymbol{F}^{p\,-1} \cdot \boldsymbol{F}^{e\,-1} = \boldsymbol{L}^{e} + \boldsymbol{L}^{p}, \text{ and} \tag{2}$$

$$\boldsymbol{L}^{p} = (1 - f^{tw}) \sum_{\alpha}^{N^{s}} \dot{\gamma}^{\alpha} (\boldsymbol{m}^{\alpha} \otimes \boldsymbol{n}^{\alpha}) + \sum_{\beta}^{N^{tw}} \dot{\gamma}^{\beta} \left(\boldsymbol{m}^{\beta} \otimes \boldsymbol{n}^{\beta}\right). \tag{3}$$

Here $\boldsymbol{L}^{p}$ is contributed by 12 {111} <110> slip systems and 12 {111} <112> twinning systems [36]. $\dot{\gamma}^{\alpha}$ and $\dot{\gamma}^{\beta}$ denote the shearing rate on the α^{th} slip system and β^{th} twinning system. $f^{tw} = \sum f^{\beta}$ is the volume fraction of all twinning systems, which can be calculated by $f^{tw} = \sum f^{\beta} = \sum \gamma^{\beta} / \gamma^{tw}$. In this equation, γ^{β} is the calculated shear strain in the β^{th} twinning system, and γ^{tw} is the reference total twinning shear strain. In FCC materials, γ^{tw} =0.707 [37]. N^{s} and N^{tw} are the numbers of slip and twinning systems, taking the value of 12. $\boldsymbol{m} \otimes \boldsymbol{n}$ is the Schmid factor**.**

According to the assumption of Kalidindi [36], only the effects between twinning and slip systems were considered in the working hardening model. The internal effects between different slip systems and twin systems were neglected. The following equations were used for the description of the shear rate:

$$\dot{\gamma}^{\alpha} = \dot{\gamma}_{0}^{\alpha} \left|\frac{\tau^{\alpha}}{g^{\alpha}}\right|^{1/m} sign(\tau^{\alpha}), \text{ and} \tag{4}$$

$$\dot{\gamma}^{\beta} = \begin{cases} \dot{\gamma}_{0}^{\beta} \left|\dfrac{\tau^{\beta}}{g^{\beta}}\right|^{1/m} & f^{tw} < 0.8\,; \\ 0 & f^{tw} = 0.8 \; or \; \tau^{\beta} \leq 0. \end{cases} \tag{5}$$

Here, $\dot{\gamma}_{0}^{\alpha}$ and $\dot{\gamma}_{0}^{\beta}$ are reference strain rates of slip and twinning. τ^{α} and τ^{β} are the corresponding resolved shear stresses. g^{α} and g^{β} are the critical resolved shear stress (CRSS) to resist slip and twinning evolution. m is the rate-sensitivity factor. The upper limit on the total volume fraction of twins is selected as 0.8 [36]. The evolution of g^{α} and g^{β} can be formlated as:

$$\dot{g}^{\alpha} = h_{s}^{\alpha} \left(1 - \frac{g^{\alpha}}{g_{s}^{\alpha}}\right) \sum \dot{\gamma}^{\alpha}, \tag{6}$$

$$h_{s}^{\alpha} = h_{s}[1 + a(f^{tw})^{b}], \tag{7}$$

$g_s^\alpha = g_0 + g_{pr}(f^{tw})^{0.5}$, and (8)

$g^\beta = \eta g^\alpha$. (9)

Here, h_s^α is the hardening rate and g_s^α is the saturated slip resistance. Following the work of Salem et al. [38] and Kalidindi [39], the effects of twinning on slip can be characterized as the effects of the total volume fraction of twinning systems on h_s^α and g_s^α of the α^{th} slip system. a, b, and η are material constants. g_0 is the saturated slip resistance in the absence of twinning and g_{pr} describes the contribution of the Hall–Petch effect.

3.2. Cohesive zone model

The constitutive relations governing the behavior of the CZM in finite element analysis are described through the utilization of a Traction Separation Law (TSL). The TSL posits a dependence of the traction force on both the normal and tangential displacements. Characterization of the CZM requires consideration of three fundamental features, including the material stiffness, a damage initiation criterion, and a damage evolution law [40]. The bi-linear TSL depicted in **Fig. 4** encompasses both the elastic and damage stages. Initially, traction strength linearly builds up as separation increases. Once it reaches the peak t_0, damages start to occur. Further separation promotes damage accumulation due to material softening. A complete material fracture occurs once the separation strength reduces to zero. The corresponding critical separation is δ_f. In this study, the maximum nominal stress criterion (MAXS) was chosen as the damage initiation criterion according to:

$$max\left\{\frac{t^n}{t_0^n}, \frac{t^s}{t_0^s}, \frac{t^t}{t_0^t}\right\}=1 \quad (10)$$

Here t_0^n, t_0^s, and t_0^t are the maximum stresses in the normal direction, the first shear direction, and the second shear direction, respectively. The energy-based damage evolution law was used by defining the damage energy G_c.

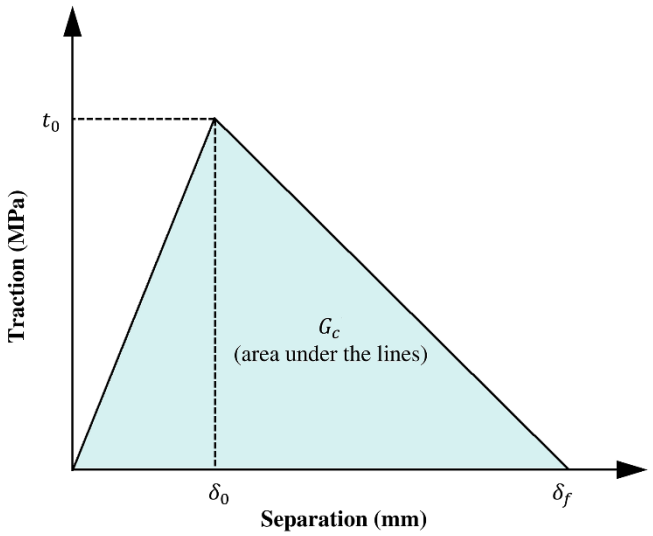

Fig. 4. Typical bi-linear traction-separation response used in CZM.

3.3. Determination of parameters in CPFEM-CZM method

For the CPFEM, most of the constitutive parameters were determined by fitting the true stress–strain and the strain-hardening curves shown in **Fig. 2**. The elastic parameters were obtained based on the work of Jia et al. [41] and Chiarodo et al. [42]. Kalilindi [39] provided the reference values of $\dot{\gamma}_0^{\alpha}$, $\dot{\gamma}_0^{\beta}$, g_0^{β} (the initial twinning resistance), a, and b in **Eqns. (4-7)**. The initial slip resistance g_0^{α} was calculated according to Li et al. [43] according to:

$$g_0^{\alpha} = \frac{1}{M}(\sigma_y + \frac{K}{\sqrt{d}}), \tag{11}$$

Here $M = 3.06$, σ_y, and $K = 304$ represent the Taylor factor, the yield stress, and the Hall-Petch coefficient, respectively. All parameters used for the CPFEM in this research are listed in **Table 2**.

Table 2. Elastic constants and hardening parameters of CuZn32 used in the CPFEM.

C_{11} (GPa)	C_{12} (GPa)	C_{44} (GPa)	$\dot{\gamma}_0^{\alpha}$ (s^{-1})	$\dot{\gamma}_0^{\beta}$ (s^{-1})	m
145	110	70	0.001	0.001	0.02
g_0^{β} (MPa)	g_{pr} (MPa)	a	b	η	

60	350	5	10	1.25
d (μm)	g_0^{α} (MPa)	g_0 (MPa)	h_s (MPa)	
17.5	60	400	200	
62.1	36	375	190	
157.7	26	360	175	

Key parameters in CZM,as listed in Table 3, were determined from uniaxial tension simulations, following the research of Wang et al. [44] and Cai et al. [37].

Table 3. Parameters used in CZM for various grain sizes.

G_C^n (MPa · mm)	G_C^s (MPa · mm)	G_C^t (MPa · mm)	
51	138	138	
d (μm)	t_0^n (MPa)	t_0^s (MPa)	t_0^t (MPa)
17.5	741	277	277
62.1	621	232	232
157.7	513	191	191

The flowchart illustrating the sequence of algorithms employed in the new CPFEM-CZM method is presented in Fig. 5.The procedure starts with the calculation of the crystal plasticity component, including slip and twinning. This calculation serves as a basis for determining whether partial or complete fracture occurs during the deformation process .

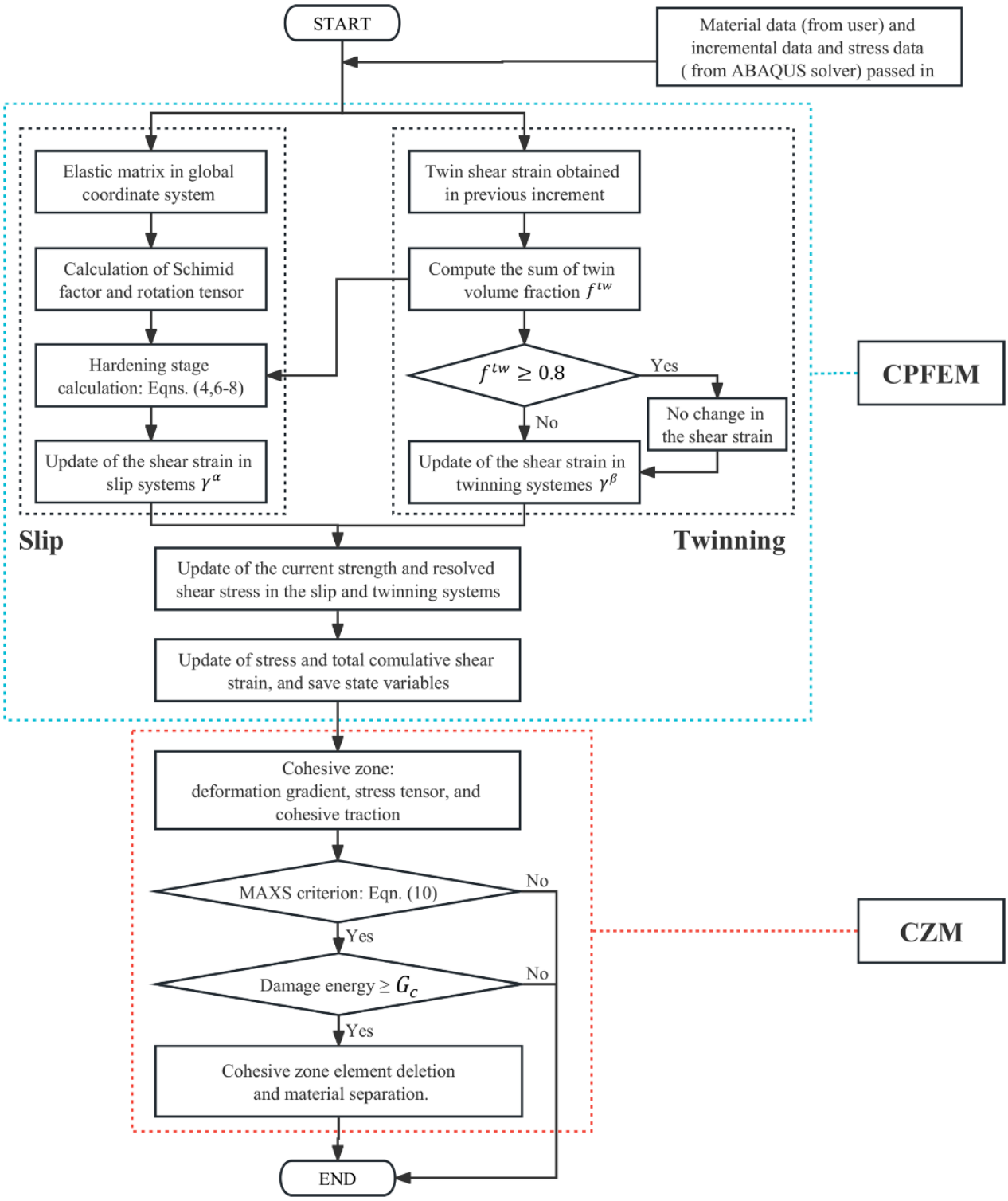

Fig. 5. The algorithm flow chart of the CPFEM-CZM method.

3.4 Modeling of Uniaxial tensile test

A series of polycrystalline RVEs were built and implemented to the uniaxial tension simulations using commercial software Abaqus, as shown in **Fig. 7**. The constitutive models and hardening model

were established via a VUMAT subroutine based on **Eqns. (1-9)** and the UMAT subroutine proposed by Huang [47]. To reduce the computational time, all RVEs of the gauge section of the specimens used in the uniaxial tensile tests have been scaled down. Furthermore, the grain sizes were averaged, and four simulations were conducted for each grain size, considering actual textures (as shown in **Fig. 6**) as well as three sets of random textures for comparison. The RVEs were modeled with C3D8 and COH3D8 types for body elements and cohesive elements, respectively,. **Fig. 8** compares the true stress-strain curves for various grain sizes. A close match of simulation and experiment results was found for samples with real textures. Simulation results for samples with random textures, which are represented in the shaded areas in **Fig. 8**, tend to exhibit larger scatter with increasing grain size. This indicates that the CPFEM-CZM method can provide a good prediction of the strain-hardening behavior in CuZn32 when real textures are considered. In the following analysis, samples with real textures are employed.

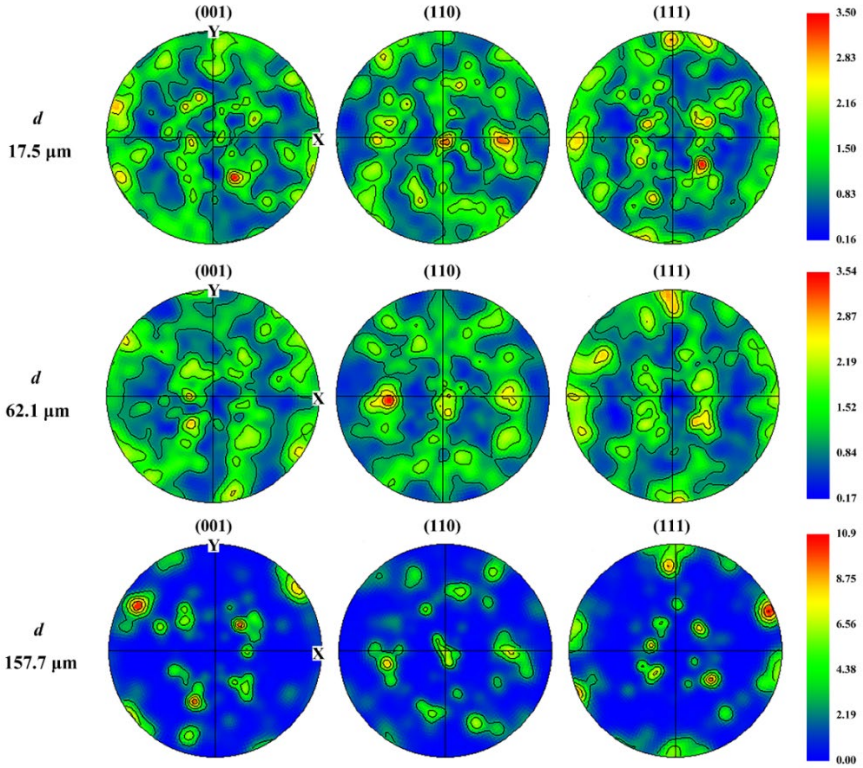

Fig. 6. Actual textures obtained from the results of EBSD for materials with different grain sizes.

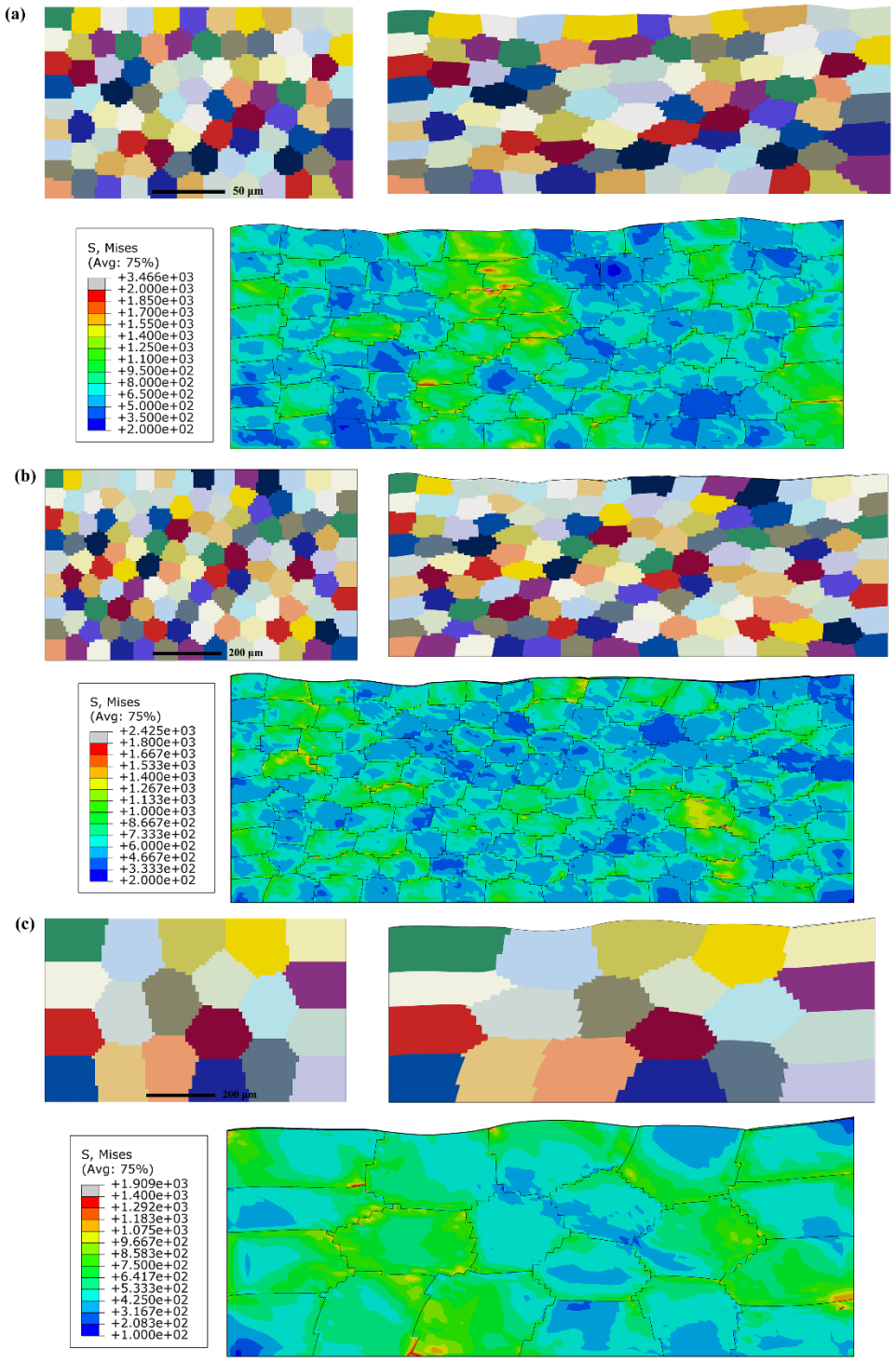

Fig. 7. Initial state and the deformed results (strain at 0.4) of RVEs under uniaxial tension with actual textures and averagegrain size of (a) 17.5 μm, (b) 62.1 μm, and (c) 157.7 μm.

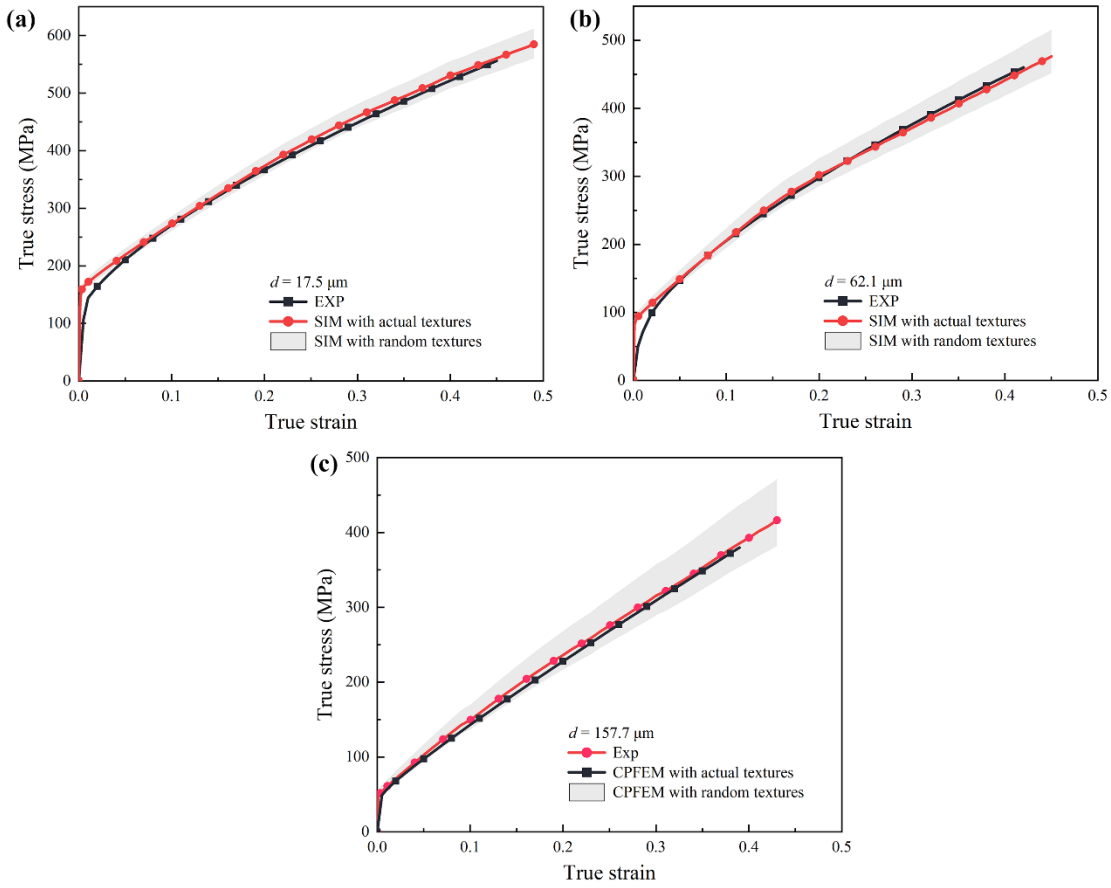

Fig. 8. Comparison of the simulated and experimental true stress–true strain curves of CuZu32 with the grain size of (a) 17.5 μm, (b) 62.1 μm, and (c) 157.7 μm.

3.5. Modeling of progressive microforming process

The progressive microforming process was modeled using both CPFEM-CZM and conventional FEM. In consideration of computational efficiency, a quarter of the system was modeled using symmetric boundary conditions. As illustrated in **Fig. 9**, conventional FEM does not account for the microstructure details of the CuZn32 sheet. Its constitutive relationship is determined from uniaxial tensile testing. The use of homogenized material properties cannot reflect the stochastic variations of material behavior. Resolving microstructure details of the entire sheet requires very fine mesh and is therefore impractical for structural scale analysis due to the high computational cost. For the CPFEM-CZM approach, considering the computational efficiency of the CPFEM, only a quarter of the deformed sheet was simulated under symmetric boundary conditions. Part of the CuZn32 sheet that is in direct contact with the punches and dies has a dimension of 1 mm in both radius and thickness, and 200 grains with an average grain size of 157.7 μm as shown in **Fig. 9(a)**. CPFEM is applied to this

region while the rest of the CuZn32 sheet follows isotropic stress-strain relationship obtained from the uniaxial tensile test in Section 2.2. To save the computational cost, cohesive elements are only embedded in regions where material shear occurs.

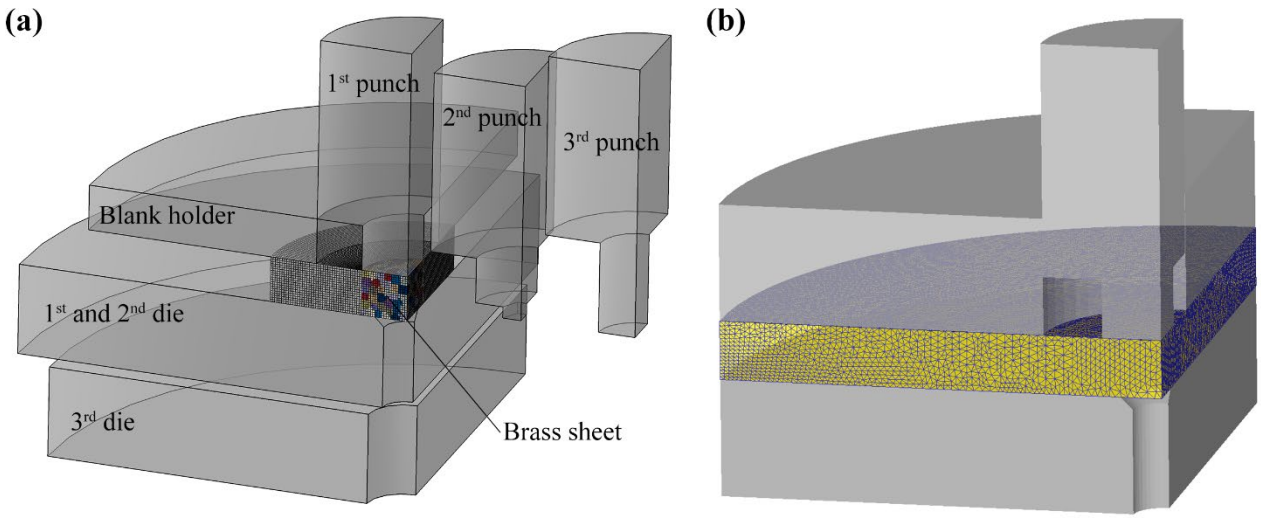

Fig. 9. Modeling of the progressive microforming process using (a) CPFEM-CZM method and (b) conventional FEM.

It is worth noting that in the CPFEM-CZM method, the distribution of the cohesive elements cannot simply be set as full-field or only on grain boundaries, as the two approaches may result in substantial discrepancies and inaccuracies in simulation results, as depicted in **Fig. 10(b)**. After several attempts, the initial distribution of cohesive elements was ultimately established as shown in **Fig. 10(a)**, utilizing COH3D8 elements. It can be concluded that good simulation results could be achieved by controlling the cohesive elements in the region where material shear potentially occurs, which is generalizable to other microstructures and shapes of parts. In regards to the initial crystal orientations, the data obtained from EBSD was insufficient to fully cover the whole model. Therefore, a hybrid way was taken, where the two symmetry surfaces parallel to the sheet thickness direction were modeled using actual texture data, while the remaining grain orientations were assigned randomly from the obtained Euler angles

library.

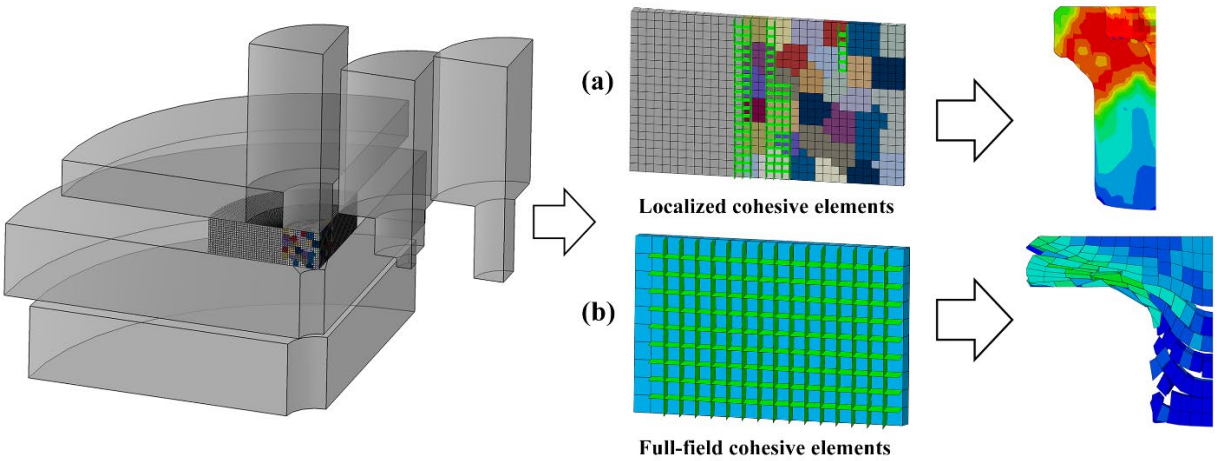

Fig. 10. Comparison between (a) localized and (b) full-field cohesive elements in sheet modeling.

4. Results and discussion

4.1. Size effect in tensile test simulation

The deformed microstructure and the distribution of von Mises stress resulting from the tensile test simulation are depicted in **Fig. 7**. Upon examining the results, several relevant insights were found. Firstly, the Hall-Petch relations at the micro-scale are observed to hold, as evidenced by the reduction in stress that ensues with an increase in grain size. Upon examination of the experimental results at 0.4 strain (**Fig. 2(a)**), the simulation and experimental results demonstrate a fracture stress ratio of approximately 1.45:1.18:1 and 1.43:1.28:1 for the three different grain sizes, respectively. This close agreement between the simulation and experimental data provides strong support for the accuracy of the proposed CPFEM approach and the corresponding parameters. Secondly, certain grains experience significantly greater deformation than others. It is found that grains experiencing higher average stress and strain tend to undergo deformation along the tensile direction and exhibit greater misorientations in relation to the surrounding grains. Lastly, the analysis reveals that stress concentration is more likely to occur around the grain boundaries of highly deformed grains due to the blocking effect of grain boundaries on dislocation motion and the consequent promotion of twin nucleation and growth in brass materials. The highest stresses are typically concentrated near grain boundaries that are oriented parallel to the direction of deformation.

4.2. Size effect on load-stroke relation

In this forming process, effective load control not only ensures product quality but also increases the longevity and cost-efficiency of the associated tooling system. Especially, the maximum value of the load will have an impact on the choice of pressure equipment, holding time, and tooling materials in mass production. During microforming, correlations between load and stroke in hexagon socket parts with various grain sizes in the three steps are illustrated in **Fig. 11(a-c)**. **Fig. 11(d)** shows the deformation of a hexagon socket part with a grain size of 157.7 μm. In this work, the average results of three sets of repeated experiments were utilized. Since only a quarter of the material was simulated, the load results of the CPFEM-CZM simulation were multiplied by four.

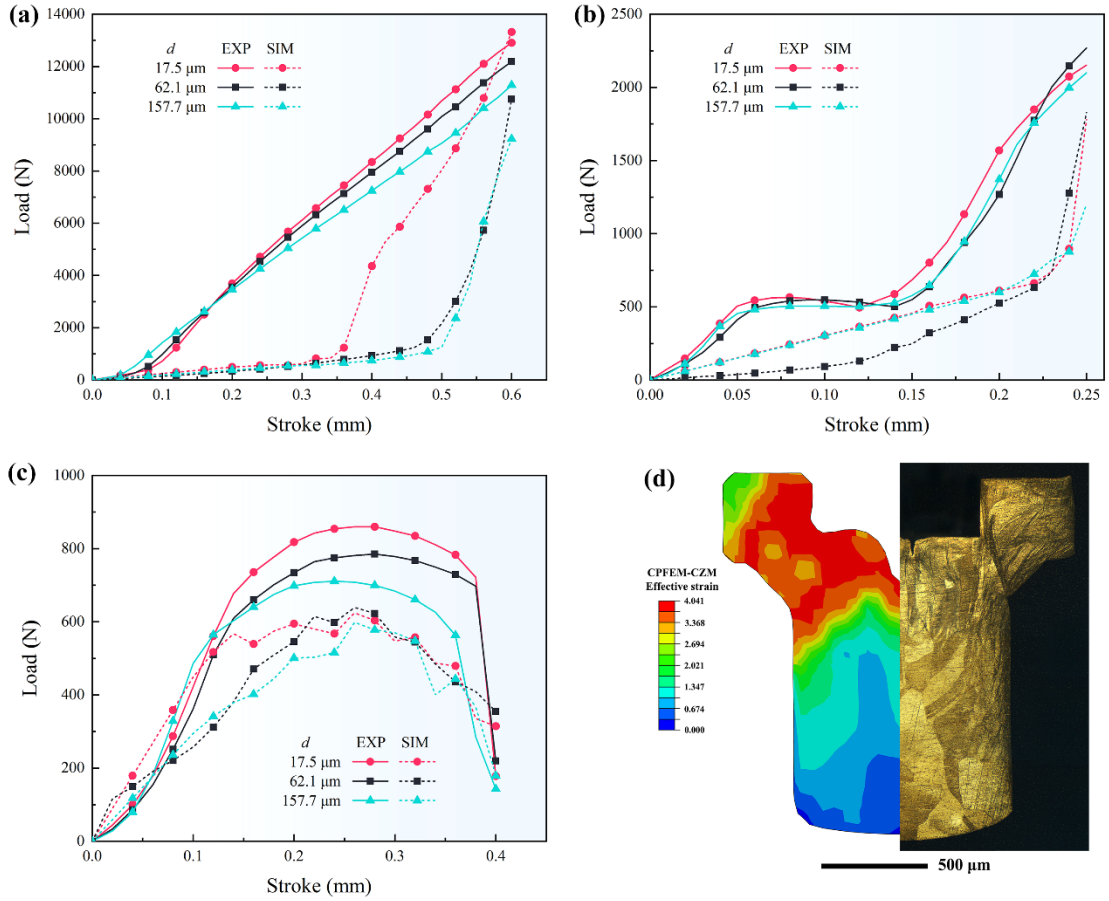

Fig. 11. Comparison of the load-stroke curves between simulations and experiments with various grain sizes in (a) step I, (b) Step II, and (c) Step III. (d) Deformation in hexagon socket part with a grain size of 157.7 μm.

It can be observed that the load in Step I is significantly greater compared to the subsequent two steps, with a difference in maximum value as much as a dozen-fold. During Step I, which involves the

first forward extrusion process, the experimental results demonstrate an essentially linear increase in load with a maximum value of approximately 11,000-13,000 N. In contrast, the simulation results exhibit slow growth and then sharply increase only during the final 0.3 mm or 0.15 mm stage as shown in **Fig. 11(a)**. During Step II, as the forming process continues, the load is initially raised to 500 N and then maintained within this range for strokes ranging from 0.06-0.15 mm. Subsequently, the load increases linearly to a range of 2,100-2,300 N. For the simulation results, a steep increase occurs in the last 0.02 mm stroke, while the maximum load is below 2,000 N. It is worth noting that Step III necessitates the full extraction of the part from the die tunnel, resulting in a much greater stroke compared to the first two steps according to **Fig. 3**. During Step III, specifically within the stroke range of 0.4-0.9 mm, only sliding friction between the punch and the shear-finished sheet material occurs. As a result, the load experiences fluctuations that are limited to the tens of Newton. Therefore, an effective stroke from 0 to 0.4 mm is employed for the analysis. As shown in **Fig. 11(c)**, load first rises in step III, and then experiences a slow increase and decrease during the continuous blanking process. After the cutting process is completed, the load abruptly drops to approximately 200 N, which is primarily generated by longitudinal sliding friction during the insertion of the part into the die tunnel. The maximum limit value for load in this progressive microforming system can be established at 15,396 N, which is the sum of the individual maximum load values for each stage: 12,907 N from Step I, 2,269 N from Step II, and 220 N from Step III. The CPFEM-CZM yields a similar prediction of (13317+1828+355=) 15,500 N. This indicates that the CPFEM-CZM can realistically predict the load limit.

The load-stroke curves also reveal various grain size effects. Specifically, the experimental results demonstrate that samples with smaller grains exhibit higher applied loads for the same stroke in every step. This trend is consistent with the conclusions in Section 4.1 as smaller grain size lead to increased stress. Secondly, in Step I (forward extrusion), the load for material with the smallest grain size (17.5 μm) exhibits a steeper increase compared to other grain sizes, indicating a delayed occurrence of fracture. In 1972, Phillips and Armstrong [48] found that the fracture strain in Brass (CuZn30) linearly decreases with $d^{-1/2}$. Nonetheless, this SE is more pronounced in the simulation than in the experiment. Besides the steep rise, there are no significant differences in load between the other two

larger grain sizes. Similarly, Zheng et al. [15] reported the load-stroke curves in CuZn35 flat pogo pins with larger initial grain sizes (71 and 107 μm) are the same compared to smaller grain sizes. This indicates that there exists a threshold grain size beyond which the load-stroke response is not affected by the extrusion operation. Thirdly, at the initial stage of the experiment, the load for coarse-grained material initially tends to be greater but is quickly surpassed by that of fine-grained material when the stroke is less than 0.15 mm and 0.1 mm for Step I and III, respectively. The observed phenomenon can be attributed to the difference in yield strain among different grain sizes. Li et al. [49] synthesized the grain size effect on yield strain for brass CuZn30 material. They found an increase in yield strain from approximately 1.95×10^{-3} to 2.2×10^{-3} when the grain size decreases from 157.7 μm to 17.5 μm. While fine-grained material is still undergoing elastic deformation, coarse-grained material has entered the plastic stage under the same stroke.

4.3. Size effect on product quality

4.3.1 Size effect on dimensional accuracy

The accuracy of dimensions in progressive formed parts holds paramount significance in the domain of product design, process development, and quality assurance. On the one hand, it is affected by process design, dimensions of the tooling system, forming speed, and various variables. On the other hand, the material characteristics and properties are more essential in microforming. The microstructure anisotropy arising from the crystalline shape, size, and orientation results in inhomogeneous deformation, which becomes increasingly pronounced with the grain size. To determine and compare the SEs on dimensional accuracy, the height and diameter distributions of key features of the hexagonal socket part were selected to examine the grain SEs on dimensional accuracy, as depicted in **Fig. 12**. The part can be divided into head, shoulder, body, and rollover features from top to bottom. The rollover, a common irregular geometry in extruded parts, was formed in the first step of this progressive microforming process and will be discussed in Section 4.3.2. Firstly, the heights of each feature were collected from the SEM results and cross-section images (**Figs. 15-17**), as shown in **Fig. 12(a)**. Two grain SEs can be summarized according to the data: (a) the scatter of every feature height increases with grain size; (b) except for rollover, the heights of all features decrease with

increasing grain size. These observations are following the conclusions of prior research by Tang et al. [7]. The design dimension of the total height was 1.7 mm, and the actual testing error is ± 0.02 mm, which is considered acceptable. Secondly, experimental measurements of the head and body diameters demonstrate different levels of scattering (**Fig. 12(b-c)**) which do not exist in the previous design. The head diameter distribution shows a gradual rising trend from top to bottom. The measured error, compared to the design size of 1.6 mm, remains substantial due to the irregular material fracture in the upper region. Thirdly, the body diameter tends to increase initially and then gradually decrease, with a slight increase at the junction with the rollover feature. The design dimension of the body diameter is 1 mm, and the results are deemed acceptable only with a grain size of 17.5 μm. The abrupt change in diameter at the very top measuring point is a consequence of necking that occurs during the second step of the process.

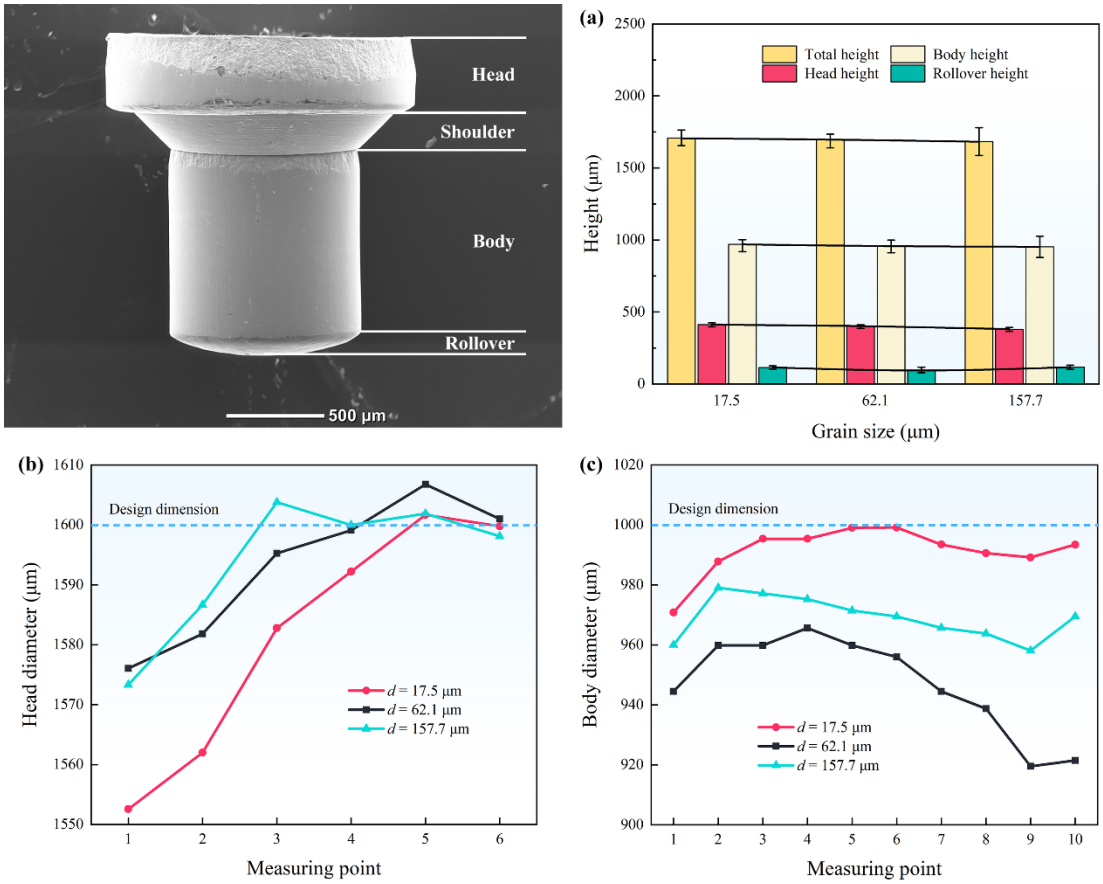

Fig. 12. The heights and diameters of various features of the formed hexagon socket part with different grain sizes.

The comparative analysis of feature dimensions in the experiments and simulations with varying grain sizes is presented in **Figs. 13-14**. The simulation results provide direct determination of heights, as demonstrated in Figs. 15-17, whereas the diameters should be twice the values mentioned earlier. The lack of distinct boundaries between the body and rollover features in the simulation results led to the integration of their heights for analytical purposes. It was determined that the majority of differences in the overall height arise from variations in the body and rollover dimensions, while the head heights remain consistent. Additionally, the presence of burr geometry, which was not considered in the simulation results, significantly contributes to the overall height. The simulation results exhibit a slight underestimation of the experimental height, and this discrepancy becomes more pronounced for coarser-grained materials. This discrepancy can be attributed to an increase in transverse material flow and a decrease in extrudate height caused by the presence of coarse grains. In the case of a limited number of grains in the direction of sheet thickness, the presence of grain inhomogeneity results in unfavorable material flow directions that deviate from the intended punching direction.. The simulation results indicate a decrease in head diameters with the rising grain size, with the middle region demonstrating minimal deviation from the experimental results and the ends demonstrating significant decreases. Unlike the head diameters, the simulation results do not reflect significant grain SE on the distribution of body diameters, while the experimental results show a decrease followed by an increase in the body diameter with increasing grain size. Interfacial friction, despite the use of identical machine oil as a lubricant, is also considered a contributing factor to grain SEs. Overall, the dimensional accuracy of the CPFEM-CZM model predictions is satisfactory, with the corresponding grain SEs being adequately reflected. **Figs. 15-17** further highlight the shortcomings of the conventional FEM simulations in terms of total height prediction, with an error of 0.1 mm and a slight overestimation of the height of the rollover feature.

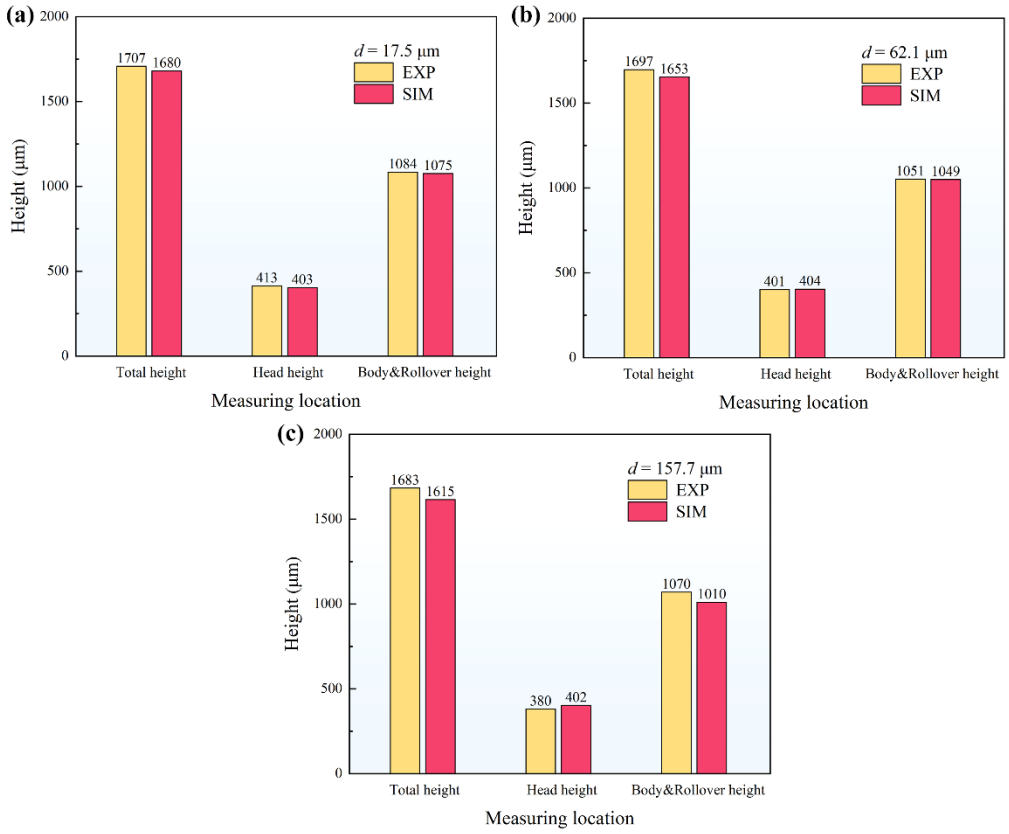

Fig. 13. The heights of various features of the simulated hexagon socket part with different grain sizes.

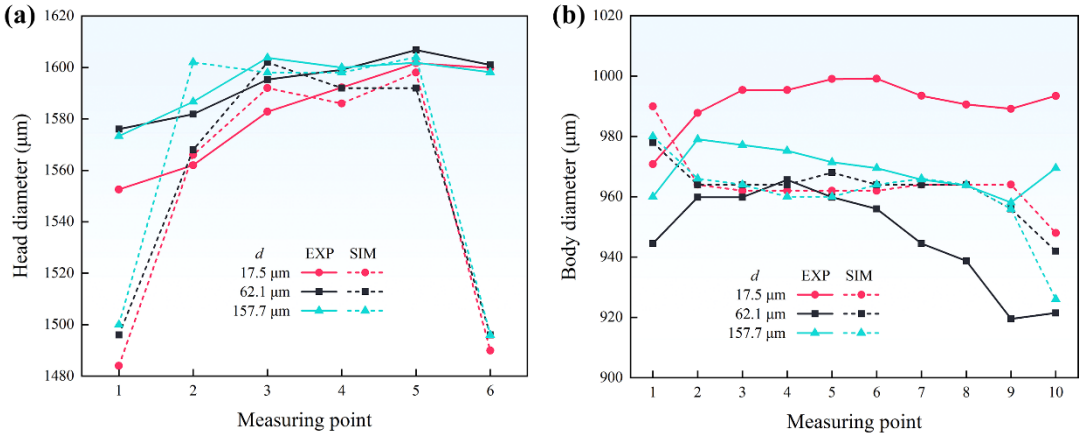

Fig. 14. The diameters of the head and body features of the simulated hexagon socket part with different grain sizes.

4.3.2 Size effect on undesirable and asymmetric geometries

Given that the microstructure evolution is closely linked to the formation of undesirable and asymmetric geometries, understanding the material flow behavior in progressive microforming process is crucial for optimizing the process and enhancing the product quality. **Figs. 15-17** depict the strain

maps and microstructure of the cross-sections, highlighting the typical inferior geometry observed in microformed parts with different initial grain sizes. It should be noted that the effective strain ε_{eq} in the conventional FEM can be directly extracted from ABAQUS, while the effective strain ε_{eq} in the CPFEM-CZM simulation needs to be calculated following the equation [50]:

$$\varepsilon_{eq} = \frac{\gamma}{\sqrt{3}} = \frac{1}{\sqrt{3}}\left[(1 - f^{tw})\sum_{\alpha}^{N^s}|\gamma^{\alpha}| + \sum_{\beta}^{N^{tw}}|\gamma^{\beta}|\right]. \tag{14}$$

The microstructural examination of the cross-sections of the resulting component reveals the presence of two salient shear bands in which the material has undergone pronounced plastic deformation and flow. Shear band I which covers the most region of the head feature was formed during the extrusion process in the first step, and then continues to develop in the second step. This shear band also dictates the material flow in the upper portion of the body. A gradual increase in the material flow line density becomes apparent when observing from the middle region of the head downwards. Shear band II, whichwas generated during the second operation, exhibits a higher flow line density in comparison to Shear band I. Shear band II appears as a series of lines of tens of micrometers, linking the bottom corner of the hexagonal socket feature to the junction between the shoulder and body portions. On both sides of the head region, four blanking shear bands were formed as a result of the second and third operations, in addition to two friction shear bands that emerged due to extrusion and friction on both sides of the body feature. The regions with intense material flow, such as the shear bands, blanking shear bands, and friction shear bands, are more accurately predicted by the CPFEM-CZM method than the conventional FEM. Elevated strain accumulation is observed in these regions. The conventional FEM fails to maintain the continuity of strain distribution, resulting in a disjointed and unrealistic strain pattern. In addition to the aforementioned shear band regions, three dead metal zones were recognized, locating at the summit of both head regions, the middle and lower portions of the body feature. A dead metal zone is characterized by a dearth of material flow. These three dead metal zones can be demarcated based on the extent of grain deformation, flow lines, and comparatively lower levels of strain accumulation as illustrated in **Figs. 15-17**. A comparison of the microstructures and flow patterns of the manufactured product with varying initial grain sizes reveals

that the area occupied by shear bands decreases as the grain size increases, contrary to the findings of Zheng et al. [15].

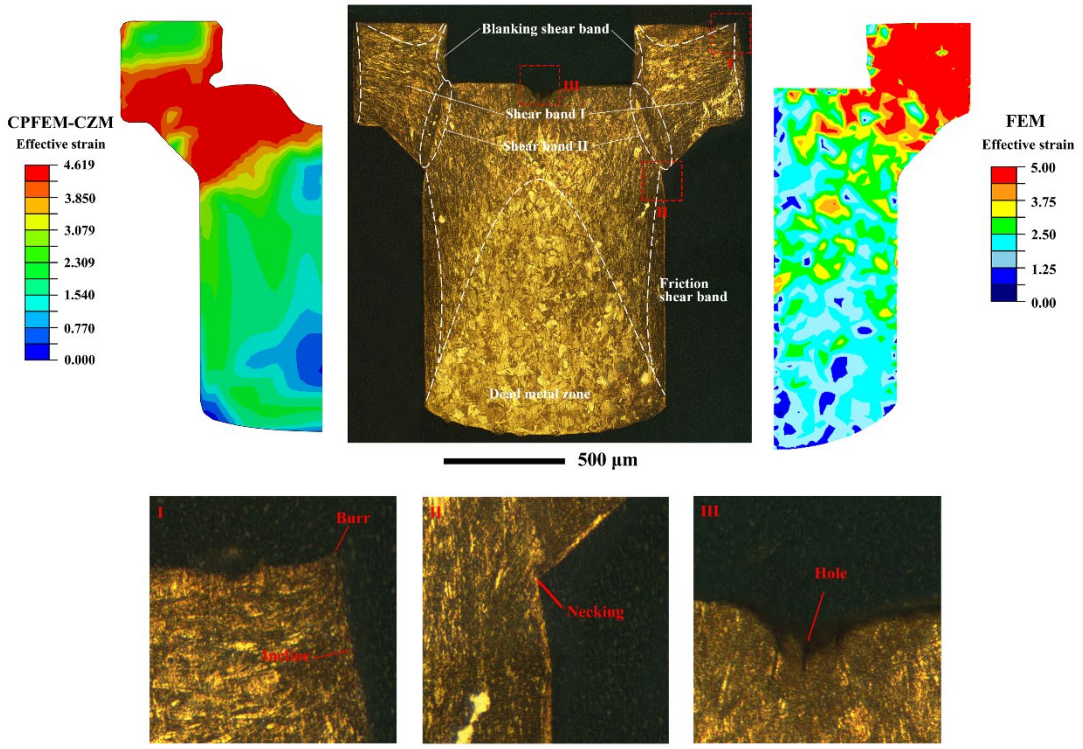

Fig. 15. Microstructures of cross section and effective strain maps of the formed part via experiment, CPFEM-CZM simulation, and conventional FEM simulation with a grain size of 17.5 μm.

The degree of asymmetry exhibited by the final component is notably pronounced, as evidenced by the SEM image depicted in **Fig. 12**, and is particularly conspicuous in the cross-section of the component with medium grain size (62.1 μm), as presented in **Fig. 16**. Given the left-right symmetry of the formed part, the asymmetry primarily manifests itself in (a) the disparity in the horizontal distance of equivalent structures from the central axis; and (b) the differential in the elevational height of equivalent structures. The positioning of the material during the experiment is contingent upon the conformity of the dies and the feature configurations established in prior stages, as well as the regulation of the feeding mechanism. In the progressive microforming process, the inadequate design of tooling tolerance and feeding velocity can lead to asymmetrical results, posing a significant challenge for simulation purposes. Addressing this challenge requires a two-fold approach: reducing tolerances and enhancing the accuracy of fit.

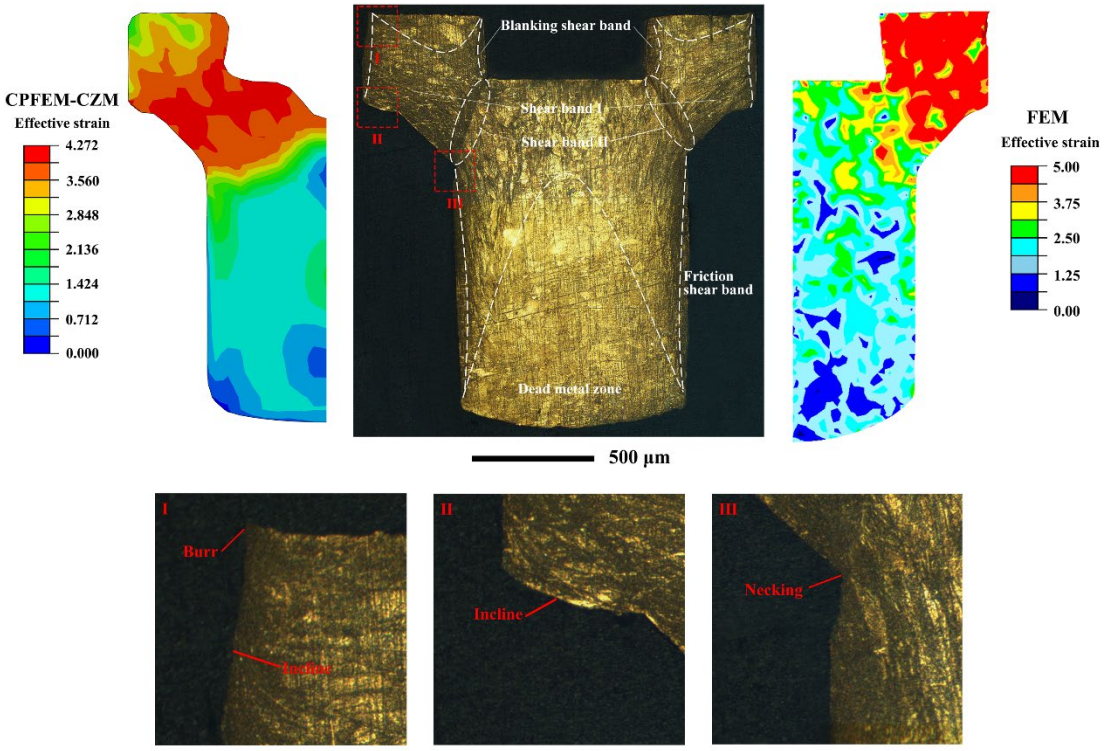

Fig. 16. Microstructures of cross section and effective strain maps of the formed part via experiment, CPFEM-CZM simulation, and conventional FEM simulation with a grain size of 62.1 μm.

The present study has identified several undesirable geometries in the formed part, which include the presence of burrs, inclines, necking, rollovers, and holes, as depicted in **Figs. 15-17**. The phenomenon of rollover is a direct consequence of the extrusion of micrograins in the first operation. In accurately predicting this phenomenon, the CPFEM-CZM approach proves to be superior compared to conventional FEM which overestimates the rollver heightThe burr and the first incline appear on the top corner and the side surfaces of the head feature during the third step. The clearance between the punch and the die in the third step is extremely small, within 0.01 mm, which precludes the presence of grain SE in the burrs. The measurements of head diameters, as shown in **Fig. 12(b)**, however, indicate that the incline angle increases with the reduction in grain size, due to the difficulties in squeezing coarser grains into the gaps between the punch and die. The second incline on the bottom corner surface of the head feature is due to the shearing of materials and the formation of a burr in the third step. The necking geometry is produced by shearing between the body and head material during the second step. It constitutes a crucial defect that requies subsequent process adjustments. Although all three corners of the head feature exhibit incline-like features, none of the aforementioned anomalies, including burrs, the two inclines, and necking, were accurately predicted by CPFEM-CZM simulations.

As shown in **Fig. 15** and **Fig. 17**, the hole defect is a common defect that occurs during the forward extrusion process, as reported by Balasundar and Raghu [51]. The hole forms during the initial extrusion step when material flows rapidly radially into the extrusion die, leading to an axial hole in the middle area of the back end of the extruded material. The formation and size of this hole were reported to be related to the angle of the chamfer angle, extrusion height, and friction conditions [51]. The width of the hole is smaller and the depth is deeper in coarser-grained material, while the position of the hole moves away from the center point with increasing grain size, as depicted in **Figs. 19-21**. CPFEM-CZM simulation demonstrate a notable capability in predicting the hole defects, which is a critical feature in progressive micromanufacturing. On the other hand, conventional FEM does not exhibit significant tendencies towards the formation of these defects, although it may generate larger hole sizes compared to the actual case. This discrepancy highlights the need for further optimization and refinement in future studies.

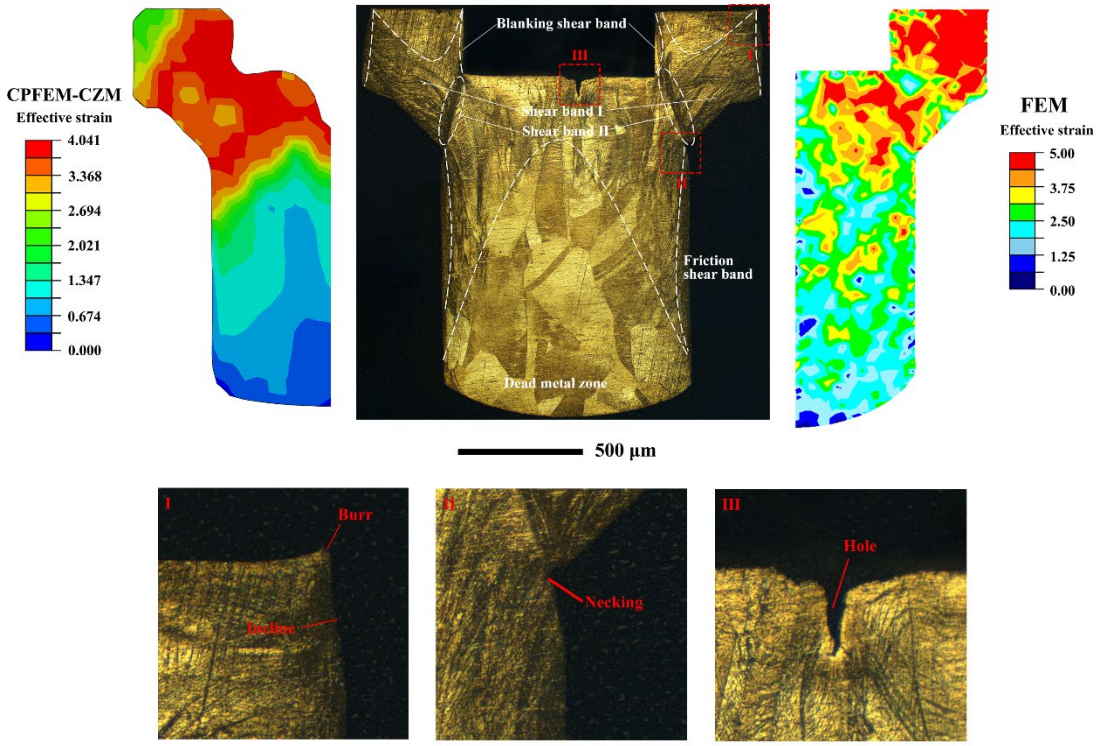

Fig. 17. Microstructures of cross section and effective strain maps of the formed part via experiment, CPFEM-CZM simulation, and conventional FEM simulation with a grain size of 157.7 μm.

4.3.3 Size effect on surface defects and quality

To study the grain SEs on surface roughening, the morphology of the surfaces on the hexagon socket

part was observed by SEM, and the surface roughness was measured by using a 3D laser scanning microscope. **Fig. 18** shows the measuring location and results of the roughness. The side surfaces of the head and body features were selected as the measurement locations, which were first tilted by an accompanying software to transform them into a plane. The roughness R_a was calculated by node coordinates obtained from the CPFEM-CZM simulation results according to:

$$R_a = \frac{1}{n}\sum_{i=1}^{n} | h_i - \bar{h}|. \tag{15}$$

Here h_i represents the distance between the selected nodes on the measuring surface and the central axis. $\bar{h}$ is the average value of h_i.

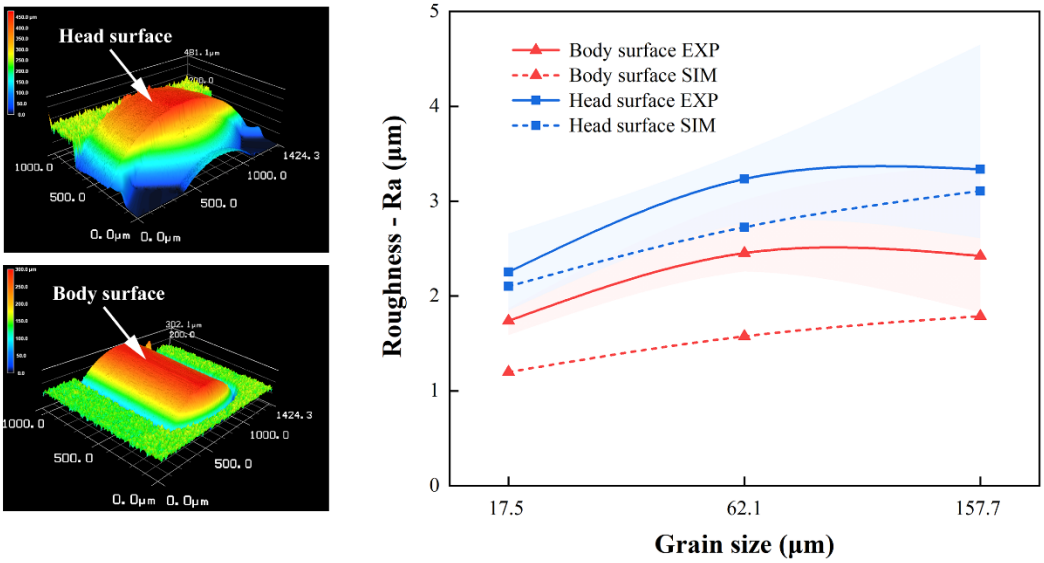

Fig. 18. Surface roughnesses of the head and body surface of the experimental and simulated parts.

Fig. 18 demonstrates the disparity in roughness between the head surface and the body surface, which is primarily attributed to the differential mechanisms of formation. The head surface is characterized by the formation of a blanking shear band, as opposed to the friction shear band that constitutes the body surface. An examination of **Fig. 19** reveals that the upper reaches of the head surface are distinctly characterized by the presence of a fracture surface feature, resulting from the material blanking process and resulting in a concomitant enhancement of roughness. In contrast, the body surface exhibits a notably smooth appearance, with minimal irregularities, except for the

occurrence of a few sporadic longitudinal fine lines. These fine lines can be attributed to the relative sliding between the material and the die during the manufacturing process. It is also observed that the surface roughness is positively correlated with the grain size. The trend mentioned above is clearly evident in the results obtained from the CPFEM-CZM simulations, albeit with magnitudes smaller in comparison to the experimental findings. The anisotropy of the grains induces incompatible strains within neighboring grains, leading to a scenario where certain grains undergo vertical deformation, while others deform in different orientations. This phenomenon ultimately gives rise to a rough surface.As the grain size increases, the surface grains are subjected to lower constraint, leading to more severe incompatible deformation of those grains and a corresponding increase in surface roughness. The error in the simulation results (shaded area) also increases with the grain size for the same reason. Moreover, the surface roughness is intricately related to the lubrication conditions. For a given sheet thickness, when the grain size increases, it leads to a reduction in the presence of lubrication pockets, resulting in an increase in friction and surface roughness. In conclusion, the roughness of the formed part is significant, and the performance of the fine-grained materials is comparatively superior. Efforts towards improving the product surface quality, such as further surface treatment of the tooling and optimized lubrication conditions, are imperative.

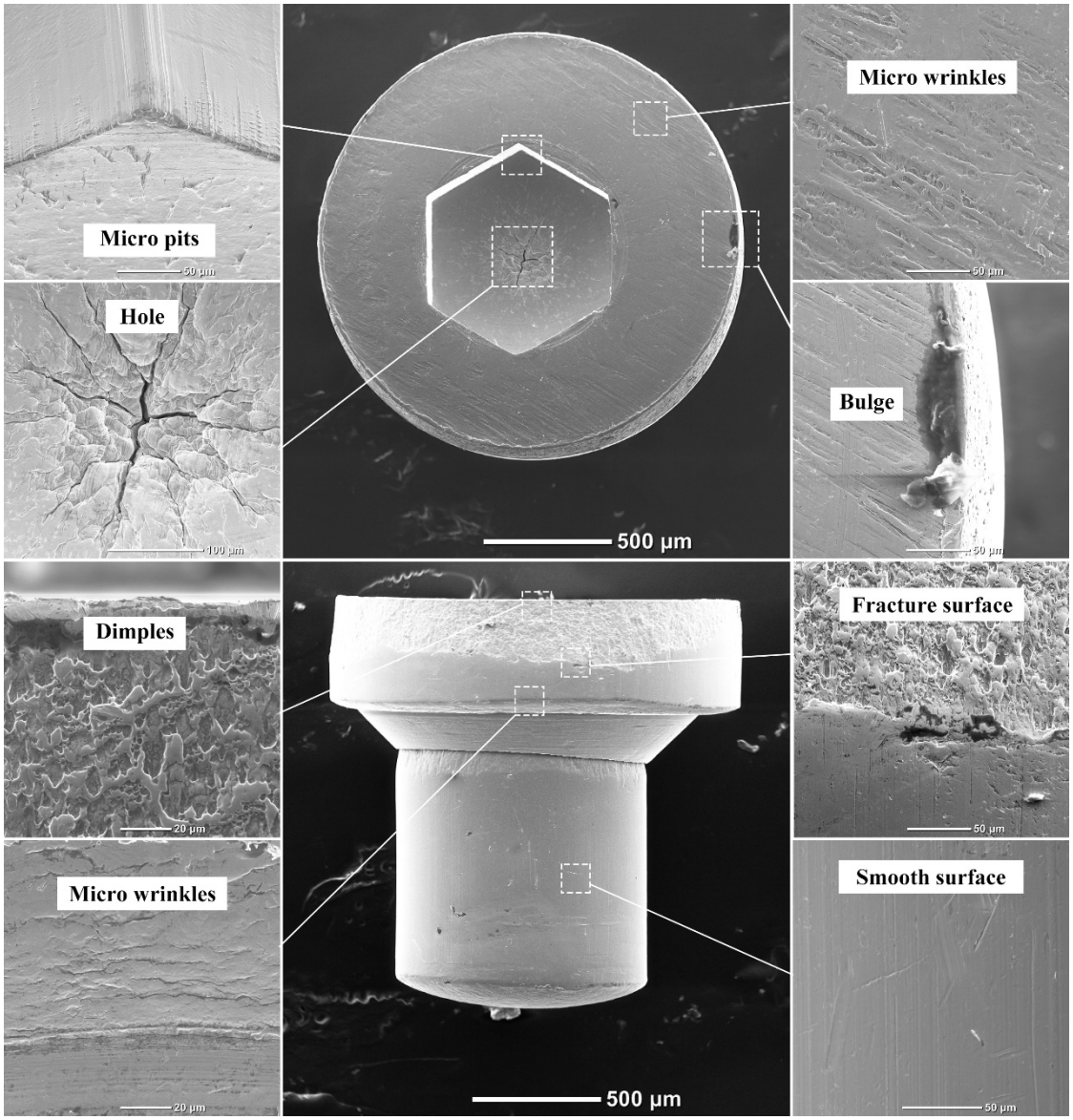

Fig. 19. Surface morphology of the micro parts with a grain size of 17.5 μm.

SEM was employed to investigate the presence and distribution of specific surface defects on the hexagon socket part. **Figs. 19-21** depict a range of flaws including micro pits, dimples, micro wrinkles, bulges, and holes. The surfaces of the body and rollover exhibit relatively smooth textures, which are a direct outcome of forward extrusion occurring parallel to the direction of the punch stroke. In contrast, fracture surfaces covering close to half of the head side surface were discovered during the examination. The dimples present on the head surfaces are indicative of ductile fracture, induced by shear stress. It was observed that the number of dimples decreased with increasing grain size, while the average size of dimples increased. This is due to the ease of dislocation movements and slips at grain boundaries,

leading to formation of dimples with high energy absorption during coordinated deformation [52]. The lower boundaries of the fracture surfaces were found to be irregular and uneven, leading to large roughness on the surface. It was discovered through examination that the head feature of the subject material possessed distinct micro wrinkles of varying morphologies on both its upper and lower surfaces. The formation of the micro wrinkles on the lower surface was attributed to the initial stage of extrusion, where the self-extrusion of the material in conjunction with the friction generated by the die led to the creation of defects of varying lengths perpendicular to the direction of the punch stroke. It was found that as the grain size increased to 157.7 μm, the wrinkles would abate, resulting in a smoother surface. Conversely, the formation of micro wrinkles on the upper surface of the head predominantly occurs as a consequence of the relative sliding between the material and punch during the initial stage. These wrinkles were exclusively observed in the outer circle of the head and were always parallel to the feed direction in the progressive microforming system. It was concluded that wrinkle defects could be prevented by optimizing lubrication conditions. In addition to the aforementioned wrinkles, micro pits were observed on the bottom surface of the hexagon socket adjacent to the hole. These micro pits were also caused by the extrusion of the material and punch and were found to be sporadically distributed and of small size. The hole defect, in addition to the previously mentioned SEs, was found to possess another grain SE observable from a top-view picture. It should be noted that as the grain size increases, the number of diffusing "branches" around the hole decreased. These "branches" are cracks formed by the coalescence of voids at high-stress locations near grain boundaries. The reduction in grain size leads to an increase in the volume fraction of the grain boundaries, which correspondingly increases the crack density. In conclusion, the presence of dimples on the side surface of the head, micro wrinkles on the lower surface of the head, and holes on the bottom surface of the hexagon socket were found to have a significant grain size tendency, while the other surface defects did not exhibit such a correlation. It is challenging to directly determine the aforementioned surface defects from the CPFEM-CZM simulations. Their presence was primarily inferred from roughness measurements in the initial stages.

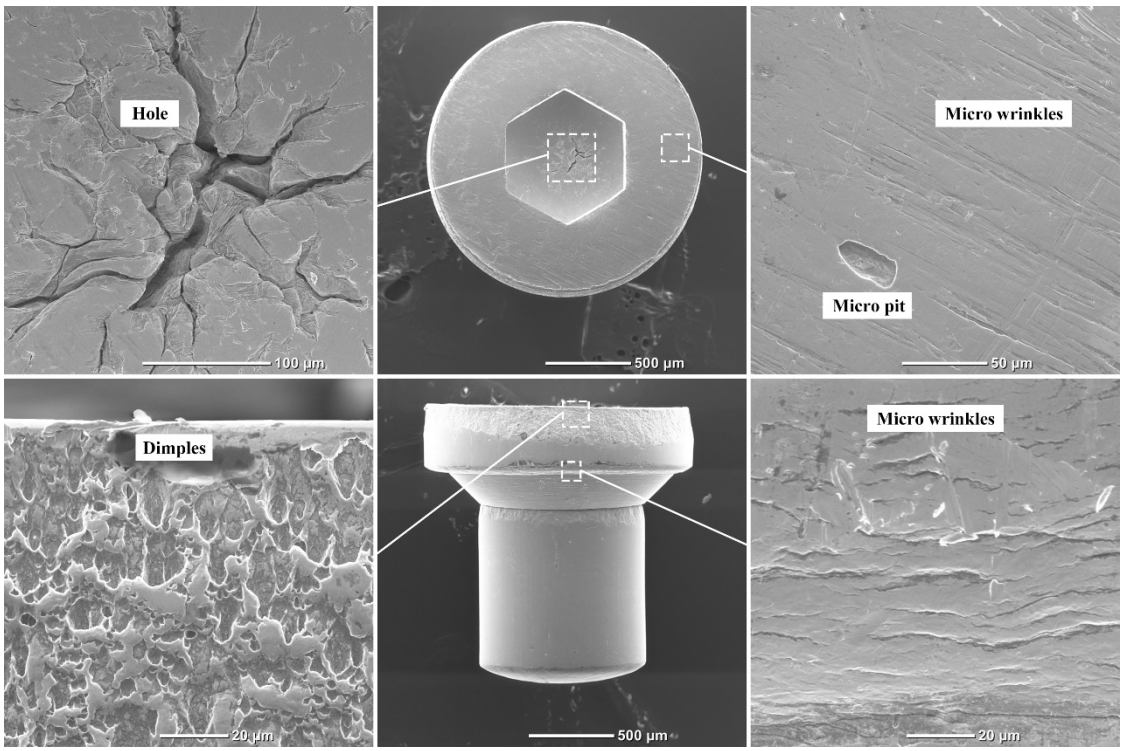

Fig. 20. Surface morphology of the micro parts with a grain size of 62.1 μm.

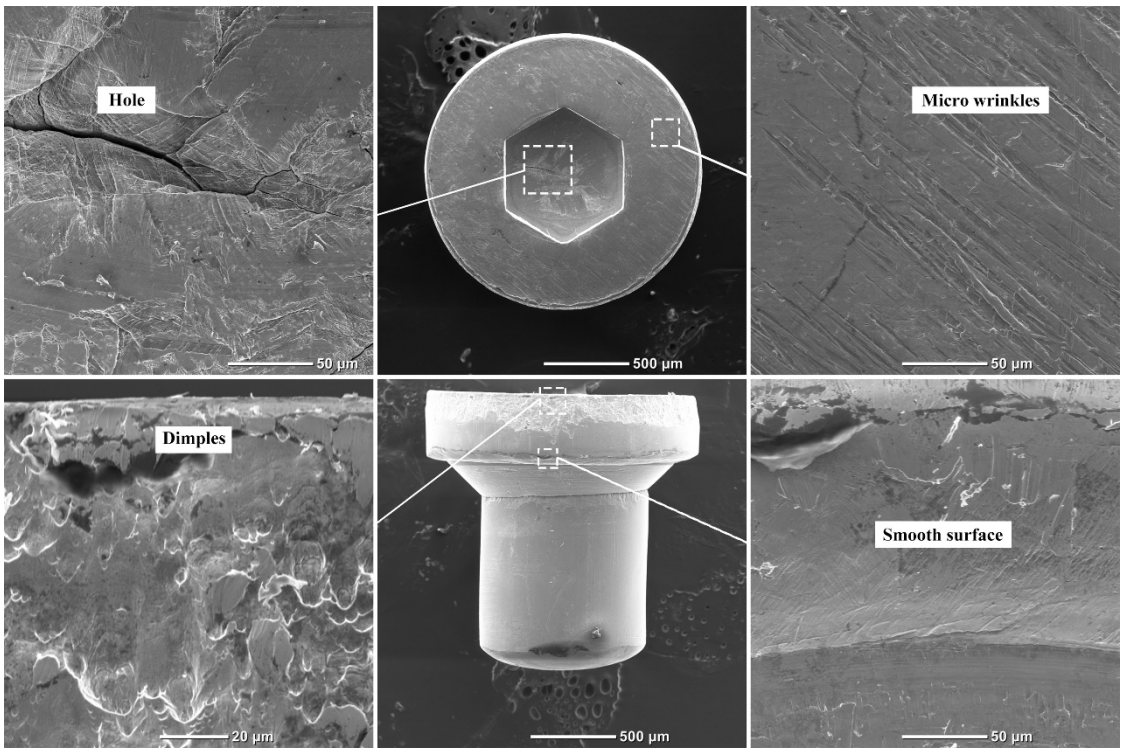

Fig. 21. Surface morphology of the micro parts with a grain size of 157.7 μm.

5. Conclusions

In this study, a novel CPFEM-CZM method is developed to investigate the grain size effect induced deformation and failure behaviors in progressive microforming. A three-step progressive microforming process was designed and implemented for the production of a hexagonal socket part as a case study with the aim at evaluating the effect of grain size on the stress and strain distribution, microstructure evolution, deformation load, dimensional accuracy, irregular geometries, and surface quality. The following conclusions were obtained:

1) Due to the complexities of the progressive microforming, a new CPFEM-CZM method was proposed for simulation and prediction: the CPFEM model incorporates the effects of slip and twinning on deformation behavior in brass materials, while the CZM considers the distribution of cohesive elements for different processes through the adoption of the bi-linear TSL and MAXS criterion. The RVEs with the actual textures of CuZn32 material with various grain sizes were simulated using this method and validated by uniaxial tensile tests; the results are in good agreement in terms of the mechanical response of the material.

2) The results showed that the CPFEM-CZM method could accurately predict the deformation load limit with different grain sizes. The CPFEM-CZM method consistently delivers results that closely match experimental observations, specifically regarding part dimensional accuracy.The total height increases with the decreasing grain size, while the head diameter is rising with grain size. Overall, the part with the initial fine-grained material has the best fit with the design scenarios in terms of its size.

3) The microstructure evolution during progressive microforming was revealed through the observation of shear bands and dead metal zones. These intricate features were accurately predicted by strain maps established using CPFEM-CZM simulations, with the size of the dead metal zones expanding as the grain size becomes coarserThe CPFEM-CZM method was able to accurately predict the hole and rollover geometries, but the results differed for the necking, the burr, and the incline geometries. The grain size-induced hole defects were found to have more branches and become narrower and deeper with the increase in grain size. Other surface defects, including

dimples, micro pits, and micro wrinkles, were found to be more prominent in coarser-grained materials. However, directly determining these defects from the CPFEM-CZM simulation results proved challenging, and their presence could only be inferred from the analysis of measured surface roughness.

In conclusion, the CPFEM-CZM method provides a robust approach for the simulation and prediction of the complex micro/meso-scale forming processes that involve elastic deformation, plastic deformation, and fracture. The methodology holds promise for the refinement of constitutive models for different materials and the distribution of cohesive elements for different processes and products in future studies.

CRediT authorship contribution statement

Xu Tong: Conceptualization, Methodology, Software, Data curation, Visualization, Writing – original draft. **Y. Li**: Conceptualization, Writing – review & editing. **M.W. Fu**: Supervision, Writing – review & editing, Project administration, Funding acquisition.

Declaration of Competing Interest

The authors declare that they have no known competing financial interests or personal relationships that could have appeared to influence the work reported in this paper.

Funding

The authors would like to acknowledge the funding support from

Yan Li would like to acknowledge the funding support from National Science Foundation under Award # OIA-2218063, as well as the start-up funds from Thayer School of Engineering at Dartmouth College.

Availability of data and material

All the data and material are available upon request to the corresponding authors.

Declaration of Competing Interest

The authors declare no competing interests.

Data availability

Data will be made available on request.

References

[1] Ghassemali E, Tan M-J, Jarfors AEW, Lim SCV. Optimization of axisymmetric open-die micro-forging/extrusion processes: An upper bound approach. Int J Mech Sci 2013;71:58-67. https://doi.org/10.1016/j.ijmecsci.2013.03.010.
[2] Wang C, Wang H, Chen G, Zhu Q, Zhang G, Cui L, Zhang P. Size effects affected uniaxial tensile properties and formability in rubber pad microforming process of pure nickel thin sheets. Int J Mech Sci 2020;182:105757. https://doi.org/10.1016/j.ijmecsci.2020.105757.
[3] Xu Z, Qiu D, Shahzamanian MM, Zhou Z, Mei D, Peng L. An improved springback model considering the transverse stress in microforming. Int J Mech Sci 2023;241:107947. https://doi.org/10.1016/j.ijmecsci.2022.107947.
[4] Wang Y, Zheng Z, Zeng F, Fu M. Geometrical and microstructural size effects in progressive forming using wires. Int J Mech Sci 2023;251:108332. https://doi.org/10.1016/j.ijmecsci.2023.108332.
[5] Ghassemali E, Tan M-J, Jarfors AEW, Lim SCV. Progressive microforming process: towards the mass production of micro-parts using sheet metal. Int J Adv Manuf 2013;66:611-21. https://doi.org/10.1007/s00170-012-4352-4.
[6] He W, Wan M, Meng B. Size effect on nonlinear unloading behavior and Bauschinger effect of Ni-based superalloy ultrathin sheet. Int J Mech Sci 2022;231:107563. https://doi.org/10.1016/j.ijmecsci.2022.107563.
[7] Tang XF, Shi SQ, Fu MW. Interactive effect of grain size and crystal structure on deformation behavior in progressive micro-scaled deformation of metallic materials. Int J Mach Tools Manuf 2020;148. https://doi.org/10.1016/j.ijmachtools.2019.103473.
[8] Meng B, Fu MW, Fu CM, Chen KS. Ductile fracture and deformation behavior in progressive microforming. Mater Des 2015;83:14-25. https://doi.org/10.1016/j.matdes.2015.05.088.
[9] Hirota K. Fabrication of micro-billet by sheet extrusion. J Mater Process Technol 2007;191:283-7. https://doi.org/10.1016/j.jmatprotec.2007.03.024.
[10] Fu MW, Chan WL. Micro-scaled progressive forming of bulk micropart via directly using sheet metals. Mater Des 2013;49:774-83. https://doi.org/10.1016/j.matdes.2013.02.045.
[11] Chan WL, Fu MW. Meso-scaled progressive forming of bulk cylindrical and flanged parts using sheet metal. Mater Des 2013;43:249-57. https://doi.org/10.1016/j.matdes.2012.07.004.
[12] Ghassemali E, Jarfors AEW, Tan M-J, Lim SCV. On the microstructure of micro-pins

manufactured by a novel progressive microforming process. Int J Mater Form 2013;6:65-74. https://doi.org/10.1007/s12289-011-1073-4.
[13] Meng B, Fu MW, Fu CM, Wang JL. Multivariable analysis of micro shearing process customized for progressive forming of micro-parts. Int J Mech Sci 2015;93:191-203. https://doi.org/10.1016/j.ijmecsci.2015.01.017.
[14] Zheng JY, Yang HP, Fu MW, Ng C. Study on size effect affected progressive microforming of conical flanged parts directly using sheet metals. J Mater Process Technol 2019;272:72-86. 10.1016/j.jmatprotec.2019.05.007.
[15] Zheng JY, Shi SQ, Fu MW. Progressive microforming of pin-shaped plunger parts and the grain size effect on its forming quality. Mater Des 2020;187. 10.1016/j.matdes.2019.108386.
[16] Esmaeilpour R, Kim H, Park T, Pourboghrat F, Xu Z, Mohammed B, Abu-Farha F. Calibration of Barlat Yld2004-18P yield function using CPFEM and 3D RVE for the simulation of single point incremental forming (SPIF) of 7075-O aluminum sheet. Int J Mech Sci 2018;145:24-41. https://doi.org/10.1016/j.ijmecsci.2018.05.015.
[17] Zhang J, Li H, Sun X, Zhan M. A multi-scale MCCPFEM framework: Modeling of thermal interface grooving and deformation anisotropy of titanium alloy with lamellar colony. Int J Plast 2020;135:102804. https://doi.org/10.1016/j.ijplas.2020.102804.
[18] Keshavarz S, Ghosh S, Reid ACE, Langer SA. A non-Schmid crystal plasticity finite element approach to multi-scale modeling of nickel-based superalloys. Acta Mater 2016;114:106-15. https://doi.org/10.1016/j.actamat.2016.05.016.
[19] Zhang H, Diehl M, Roters F, Raabe D. A virtual laboratory using high resolution crystal plasticity simulations to determine the initial yield surface for sheet metal forming operations. Int J Plast 2016;80:111-38. https://doi.org/10.1016/j.ijplas.2016.01.002.
[20] Asim UB, Siddiq MA, Kartal ME. A CPFEM based study to understand the void growth in high strength dual-phase titanium alloy (Ti-10V-2Fe-3Al). Int J Plast 2019;122:188-211. https://doi.org/10.1016/j.ijplas.2019.07.002.
[21] Cao J, Zhuang W, Wang S, Lin J. Development of a VGRAIN system for CPFE analysis in micro-forming applications. Int J Adv Manuf 2010;47:981-91. https://doi.org/10.1007/s00170-009-2135-3.
[22] Guo N, Wang J, Sun CY, Zhang YF, Fu MW. Analysis of size dependent earing evolution in micro deep drawing of TWIP steel by using crystal plasticity modeling. Int J Mech Sci 2020;165:105200. https://doi.org/10.1016/j.ijmecsci.2019.105200.
[23] Tong X, Zheng J-Y, Fu MW. Numerical and experimental study of the size effect on deformation behavior and quality of microembossed multi-channel structures. J Manuf Processes 2022;78:363-75. https://doi.org/10.1016/j.jmapro.2022.04.047.
[24] Kim J-B, Yoon JW. Necking behavior of AA 6022-T4 based on the crystal plasticity and damage models. Int J Plast 2015;73:3-23. https://doi.org/10.1016/j.ijplas.2015.06.013.
[25] Liu J, Huang M, Li Z, Zhao L, Zhu Y. Microvoid growth mechanism in FCC polycrystals and a statistical damage model. Int J Plast 2021;137:102888. https://doi.org/10.1016/j.ijplas.2020.102888.
[26] Liu Q, Roy A, Tamura S, Matsumura T, Silberschmidt VV. Micro-cutting of single-crystal metal: Finite-element analysis of deformation and material removal. Int J Mech Sci 2016;118:135-43. https://doi.org/10.1016/j.ijmecsci.2016.09.021.
[27] Wang Z, Zhang J, Xu Z, Zhang J, Hassan Hu, Li G, Zhang H, Hartmaier A, Fang F, Yan Y, Sun T. Crystal plasticity finite element modeling and simulation of diamond cutting of polycrystalline copper.

J Manuf Processes 2019;38:187-95. https://doi.org/10.1016/j.jmapro.2019.01.007.
[28] Zhang D, Li H, Guo X, Yang Y, Yang X, Feng Z. An insight into size effect on fracture behavior of Inconel 718 cross-scaled foils. Int J Plast 2022;153:103274. https://doi.org/10.1016/j.ijplas.2022.103274.
[29] Elices M, Guinea GV, Gómez J, Planas J. The cohesive zone model: advantages, limitations and challenges. Eng Fract Mech 2002;69:137-63. https://doi.org/10.1016/S0013-7944(01)00083-2.
[30] Xu X-P, Needleman A. Void nucleation by inclusion debonding in a crystal matrix. Modell Simul Mater Sci Eng 1993;1:111. https://doi.org/10.1088/0965-0393/1/2/001.
[31] Phan V-T, Zhang X, Li Y, Oskay C. Microscale modeling of creep deformation and rupture in Nickel-based superalloy IN 617 at high temperature. Mech Mater 2017;114:215-27. https://doi.org/10.1016/j.mechmat.2017.08.008.
[32] Zhao N, Wang W, Liu Y. Intergranular mechanical behavior in a blade groove-like component by crystal plasticity model with cohesive zone model. Eng Fract Mech 2018;201:196-213. https://doi.org/10.1016/j.engfracmech.2018.06.031.
[33] Yalçinkaya T, Özdemir İ, Firat AO. Inter-granular cracking through strain gradient crystal plasticity and cohesive zone modeling approaches. Theor Appl Fract Mech 2019;103:102306. https://doi.org/10.1016/j.tafmec.2019.102306.
[34] Liu L-Y, Yang Q-S, Liu X, Nian X-C. Crystal cracking of grain-gradient aluminum by a combined CPFEM-CZM method. Eng Fract Mech 2021;242:107507. https://doi.org/10.1016/j.engfracmech.2020.107507.
[35] Li L, Liu W, Qi F, Wu D, Zhang Z. Effects of deformation twins on microstructure evolution, mechanical properties and corrosion behaviors in magnesium alloys - A review. J Magnesium Alloys 2022;10:2334-53. https://doi.org/10.1016/j.jma.2022.09.003.
[36] Kalidindi SR. Incorporation of deformation twinning in crystal plasticity models. J Mech Phys Solids 1998;46:267-90. https://doi.org/10.1016/S0022-5096(97)00051-3.
[37] Cai W, Sun C, Wang C, Qian L, Li Y, Fu MW. Modelling of the intergranular fracture of TWIP steels working at high temperature by using CZM–CPFE method. Int J Plast 2022;156:103366. https://doi.org/10.1016/j.ijplas.2022.103366.
[38] Salem AA, Kalidindi SR, Semiatin SL. Strain hardening due to deformation twinning in α-titanium: Constitutive relations and crystal-plasticity modeling. Acta Mater 2005;53:3495-502. https://doi.org/10.1016/j.actamat.2005.04.014.
[39] R. Kalidindi S. Modeling anisotropic strain hardening and deformation textures in low stacking fault energy fcc metals. Int J Plast 2001;17:837-60. https://doi.org/10.1016/S0749-6419(00)00071-1.
[40] Lu M, Wang F, Zeng X, Chen W, Zhang J. Cohesive zone modeling for crack propagation in polycrystalline NiTi alloys using molecular dynamics. Theor Appl Fract Mech 2020;105:102402. https://doi.org/10.1016/j.tafmec.2019.102402.
[41] Jia N, Roters F, Eisenlohr P, Kords C, Raabe D. Non-crystallographic shear banding in crystal plasticity FEM simulations: Example of texture evolution in α-brass. Acta Mater 2012;60:1099-115. https://doi.org/10.1016/j.actamat.2011.10.047.
[42] Chiarodo R, Spain I, Bolsaitis P. Elastic constants and their pressure derivatives of α-brass single crystals. J Phys Chem Solids 1974;35:762-4. https://doi.org/10.1016/S0022-3697(74)80234-9.
[43] Li K, Yu B, Misra RDK, Han G, Tsai YT, Shao CW, Shang CJ, Yang JR, Zhang ZF. Strain rate dependence on the evolution of microstructure and deformation mechanism during nanoscale

deformation in low carbon-high Mn TWIP steel. Mater Sci Eng A 2019;742:116-23. https://doi.org/10.1016/j.msea.2018.11.006.
[44] Wang YJ, Ru CQ. Determination of two key parameters of a cohesive zone model for pipeline steels based on uniaxial stress-strain curve. Eng Fract Mech 2016;163:55-65. https://doi.org/10.1016/j.engfracmech.2016.06.017.
[45] Koster W, Rauscher W. Relations between the modulus of elasticity of binary alloys and their structure. In, 1951,
[46] Kumar R, Misra A. Some basic aspects of electromagnetic radiation emission during plastic deformation and crack propagation in Cu–Zn alloys. Mater Sci Eng A 2007;454-455:203-10. https://doi.org/10.1016/j.msea.2006.11.011.
[47] Huang Y. A user-material subroutine incroporating single crystal plasticity in the ABAQUS finite element program. Harvard Univ. Cambridge; 1991.
[48] Phillips WL, Armstrong RW. The strain dependence of the flow stress-grain size relation for 70:30 brass. Metallurgical Transactions 1972;3:2571-7. https://doi.org/10.1007/BF02644231.
[49] Li D, Wang L, Li W. Effects of grain size from micro scale to nanoscales on the yield strain of brass under compressive and tensile stresses using a Kelvin probing technique. Mater Sci Eng A 2004;384:355-60. https://doi.org/10.1016/j.msea.2004.06.060.
[50] Shrivastava SC, Jonas JJ, Canova G. Equivalent strain in large deformation torsion testing : Theoretical and practical considerations. J Mech Phys Solids 1982;30:75-90. https://doi.org/10.1016/0022-5096(82)90014-X.
[51] Balasundar I, Raghu T. Investigations on the extrusion defect – Axial hole or funnel. Mater Des 2010;31:2994-3001. https://doi.org/10.1016/j.matdes.2010.01.027.
[52] Qin W, Li J, Liu Y, Kang J, Zhu L, Shu D, Peng P, She D, Meng D, Li Y. Effects of grain size on tensile property and fracture morphology of 316L stainless steel. Mater Lett 2019;254:116-9. https://doi.org/10.1016/j.matlet.2019.07.058.